

**Feasibility study on the use of  
Trigger-Object Level Analysis in the Search  
for the Standard Model Higgs boson  
produced by vector-boson fusion and  
decaying to bottom quarks with the ATLAS  
detector.**

Andrew J Strange

School of Physics and Astronomy



2018

A dissertation submitted to the University of Manchester  
for the degree of Master of Science by Research  
in the Faculty of Science and Engineering

# CONTENTS

<b>Contents</b>	<b>2</b>
<b>List of Figures</b>	<b>4</b>
<b>List of Tables</b>	<b>6</b>
<b>Abstract</b>	<b>7</b>
<b>Declaration</b>	<b>8</b>
<b>Copyright Statement</b>	<b>9</b>
<b>Acknowledgements</b>	<b>10</b>
<b>1 Introduction</b>	<b>11</b>
<b>2 Theory</b>	<b>14</b>
2.1 Standard Model . . . . .	14
2.2 Physics of $pp$ Collisions . . . . .	19
2.3 The Higgs Boson . . . . .	22
<b>3 Detector</b>	<b>27</b>
3.1 The Large Hadron Collider . . . . .	27
3.2 The ATLAS Detector . . . . .	29
3.3 Trigger and Data Acquisition . . . . .	32
3.4 Event Cleaning . . . . .	33
3.5 Object Reconstruction . . . . .	34
3.6 Trigger-Object Level Analysis . . . . .	38
<b>4 Event Selection</b>	<b>40</b>
4.1 ATLAS Event Data . . . . .	40
4.2 Datasets . . . . .	41
4.3 Monte-Carlo simulated events . . . . .	41
4.4 Jet Extraction . . . . .	42
4.5 VBF $H \rightarrow b\bar{b}$ Analysis Strategy . . . . .	43
<b>5 Object Performance</b>	<b>45</b>
5.1 Leading $b$ -jets . . . . .	46

5.2	Leading Non $b$ -jets . . . . .	50
5.3	Jet Tagging Efficiency . . . . .	54
5.4	Summary . . . . .	57
<b>6</b>	<b>VBF <math>H \rightarrow b\bar{b}</math> Analysis</b>	<b>58</b>
6.1	Cutflow . . . . .	58
6.2	Specific Jet Feature Distributions . . . . .	62
6.3	Kinematic quantities of the VBF $H \rightarrow b\bar{b}$ event . . . . .	66
6.4	BDT Input Variables . . . . .	68
6.5	Summary . . . . .	70
<b>7</b>	<b>Conclusions</b>	<b>71</b>
<b>A</b>	<b>Configuration</b>	<b>74</b>
A.1	Files . . . . .	74
A.2	Configurations . . . . .	75
<b>B</b>	<b>Boosted Decision Trees</b>	<b>76</b>
B.1	Machine Learning . . . . .	76
B.2	VBF $H \rightarrow b\bar{b}$ BDT Training . . . . .	77
	<b>Bibliography</b>	<b>78</b>

*Word Count: 16997*

## LIST OF FIGURES

2.1	Feynmann diagrams of lowest order Higgs production processes . . . . .	23
2.2	Higgs production cross section as a function of Higgs mass at a $\sqrt{s} = 14$ TeV . . . . .	24
3.1	Schematic cut-away of the ATLAS detector . . . . .	29
3.2	Schematic plot of the ATLAS Trigger and Data acquisition system . . . . .	32
5.1	$\Delta R$ values for online/offline jet pairs in Monte-Carlo simulation . . . . .	45
5.2	$\frac{\Delta p_T}{p_T}$ for the leading $b$ -jet in data and Monte-Carlo simulations . . . . .	47
5.3	$\frac{\Delta p_T}{p_T}$ distribution for leading $b$ -jets with $89 < p_T < 91$ GeV in data and Monte-Carlo simulations . . . . .	48
5.4	$\frac{\Delta \eta}{\eta}$ for the leading $b$ -jet in data and Monte-Carlo simulations . . . . .	49
5.5	$\frac{\Delta \phi}{\phi}$ for the leading $b$ -jet in data and Monte-Carlo simulations . . . . .	49
5.6	$\frac{\Delta p_T}{p_T}$ for the leading $p_T$ non- $b$ -jet in data and Monte-Carlo simulations . . . . .	50
5.7	$\frac{\Delta p_T}{p_T}$ distribution for leading non- $b$ -jets with $89 < p_T < 91$ GeV in data and Monte-Carlo simulations . . . . .	51
5.8	$\frac{\Delta \eta}{\eta}$ for the leading non- $b$ -jet in data and Monte-Carlo simulations . . . . .	52
5.9	$\frac{\Delta \phi}{\phi}$ for the leading non- $b$ -jet in data and Monte-Carlo simulations . . . . .	53
5.10	Comparison of $b$ -jet tagging efficiency on truth $b$ -jets between online and offline jets in Monte-Carlo simulation . . . . .	55
5.11	Comparison of mistag rate between online and offline truth $c$ -jets in Monte-Carlo simulation . . . . .	56
5.12	Comparison of mistag rate between online and offline truth light-jets in Monte-Carlo simulation . . . . .	57
6.1	VBF $H \rightarrow b\bar{b}$ Cutflow ratio for Monte-Carlo simulation . . . . .	59
6.2	VBF $H \rightarrow b\bar{b}$ Cutflow ratio for data . . . . .	60
6.3	$p_T$ distribution of the leading $b$ -jet of the VBF $H \rightarrow b\bar{b}$ event . . . . .	62
6.4	$p_T$ distribution of the leading non- $b$ -jet of the VBF $H \rightarrow b\bar{b}$ event . . . . .	63
6.5	$\eta$ distribution of the leading $b$ -jet of the VBF $H \rightarrow b\bar{b}$ event . . . . .	64
6.6	$\eta$ distribution of the leading non- $b$ -jet of the VBF $H \rightarrow b\bar{b}$ event . . . . .	65
6.7	Comparison of the $p_{Tjj}$ distribution of the VBF $H \rightarrow b\bar{b}$ events for HLT and offline objects . . . . .	66
6.8	Comparison of the $m_{jj}$ distribution of the VBF $H \rightarrow b\bar{b}$ events for HLT and offline objects . . . . .	66
6.9	Comparison of the $p_{Tbb}$ distribution of the VBF $H \rightarrow b\bar{b}$ events for HLT and offline objects . . . . .	67

6.10	Comparison of the $m_{bb}$ distribution of the VBF $H \rightarrow b\bar{b}$ events for HLT and offline objects . . . . .	68
6.11	Comparison of the $\eta^*$ distribution of the VBF $H \rightarrow b\bar{b}$ events for HLT and offline objects . . . . .	69
6.12	Comparison of the $p_{Tbalance}$ distribution of the VBF $H \rightarrow b\bar{b}$ events for HLT and offline objects . . . . .	69

## LIST OF TABLES

2.1	Properties of Spin- $\frac{1}{2}$ quarks . . . . .	15
2.2	Properties of Spin- $\frac{1}{2}$ leptons . . . . .	15
2.3	Properties of Spin-1 gauge bosons . . . . .	16
2.4	Branching ratios of SM Higgs boson with $m_H = 125$ GeV . . . . .	25
3.1	Performance goals and operational ranges of the ATLAS detector . . . . .	31
4.1	<i>Two-central</i> channel event cuts . . . . .	44
5.1	Pseudorapidity bands of the object performance analysis . . . . .	46
6.1	Results cutflow for the <i>two-central</i> VBF $H \rightarrow b\bar{b}$ events . . . . .	59
6.2	Signal/Background definition $m_{bb}$ values . . . . .	62
A.1	Full filenames of samples and other files used during the analysis . . . . .	74
A.2	Full names of configurations used during the analysis . . . . .	75
B.1	BDT Variables used in training for the VBF $H \rightarrow b\bar{b}$ analysis. . . . .	77

# ABSTRACT

This dissertation presents a feasibility study on the application of Trigger-Object Level Analysis (TLA) to the search for the Standard Model Higgs boson produced by Vector Boson Fusion (VBF) and decaying to b-quarks, using  $4.6 \text{ fb}^{-1}$  of proton-proton collision data taken at a centre-of-mass energy of 13 TeV by the ATLAS detector. The VBF process is predicted to be the second largest cross-section process at the Large Hadron Collider, and searches for the VBF produced Higgs decaying to  $b\bar{b}$  exploit the characteristic final state topology to select events. TLA refers to the procedure of only storing the jet objects reconstructed at the trigger-level of the ATLAS detector for use in analysis, which permits an increase in the output rate of the detector, as a result of reducing the byte size of the detector readout.

This dissertation suggests that a TLA approach is feasible for the VBF  $H \rightarrow b\bar{b}$  channel. The analysis showed that the behaviour of trigger-level jets was comparable to that of the standard reconstructed jets, and the agreement of the jet kinematic properties could be improved by applying trigger-level calibrations. Simulating the VBF  $H \rightarrow b\bar{b}$  analysis using trigger-level objects resulted in a 20% reduction in the number of final events for the TLA compared to the standard analysis, which shows that the 100% detector output rate increase from the current TLA approach would produce an overall increase in the number of final state events. Select kinematic properties of the VBF  $H \rightarrow b\bar{b}$  final state were studied and shown to demonstrate comparable behaviour between the trigger-level and standard reconstructed objects.

## DECLARATION

No portion of the work referred to in the dissertation has been submitted in support of an application for another degree or qualification of this or any other university or other institute of learning.

Andrew Strange



## COPYRIGHT STATEMENT

The author of this dissertation (including any appendices and/or schedules to this dissertation) owns certain copyright or related rights in it (the "Copyright") and he has given The University of Manchester certain rights to use such Copyright, including for administrative purposes.

Copies of this dissertation, either in full or in extracts and whether in hard or electronic copy, may be made only in accordance with the Copyright, Designs and Patents Act 1988 (as amended) and regulations issued under it or, where appropriate, in accordance with licensing agreements which the University has from time to time. This page must form part of any such copies made.

The ownership of certain Copyright, patents, designs, trademarks and other intellectual property (the "Intellectual Property") and any reproductions of copyright works in the dissertation, for example graphs and tables ("Reproductions"), which may be described in this dissertation, may not be owned by the author and may be owned by third parties. Such Intellectual Property and Reproductions cannot and must not be made available for use without the prior written permission of the owner(s) of the relevant Intellectual Property and/or Reproductions.

Further information on the conditions under which disclosure, publication and commercialisation of this dissertation, the Copyright and any Intellectual Property and/or Reproductions described in it may take place is available in the University IP Policy, in any relevant Dissertation restriction declarations deposited in the University Library, The University Library's regulations and in The University's policy on Presentation of Dissertations

## ACKNOWLEDGEMENTS

This dissertation has been produced with guidance and support from many people, without which it would not have seen the light of day.

Primarily, I must thank my supervisor Andy Pilkington. His guiding hand and experience over the course of this project has at times been the only thing keeping it on the straight and narrow. I am indebted to his help and his willingness to put up with me over the course of this year, and this work is built around the backbone he provided.

Secondly, thanks to the Manchester Particle Physics group, for providing a terrific environment for work, for all of the guidance and for all of the socialising. Particular mention must go to my colleagues on the ATLAS project; Jacob, Jonathan, Yaadav and Agni for all of their invaluable experience and assistance throughout the year. Additionally, I must thank Sabah for providing me with his help and knowledge without hesitation when I needed it.

From my time at undergraduate, I must thank all my friends, who provided encouragement and support from all the myriad of locations around the world they've run off to. Also I must thank Lisa Jardine-Wright, Dave Green and especially Barry Phipps for all of their advice during my time under their watch and thank Dave for permitting me to use his L<sup>A</sup>T<sub>E</sub>X template.

Finally however, none of this would have occurred were it not for the support of my dad, mum and brother. Their unwavering and tireless support, endless encouragement, motivating prods and willingness to put up with whatever inconvenience I could give them carried this work through to its close.

To all those mentioned here, I owe you the most sincere gratitude. Thank you for everything.

## INTRODUCTION

Modern understanding of particle physics is best described by the Standard Model (SM), a theoretical framework describing the behaviour and interactions of all known fundamental particles. The Standard Model covers three of the four fundamental forces, omitting gravitational interactions, and has been thoroughly explored with decades of experimental observations showing good agreement with its predictions. Within the theory of the Standard Model, it is postulated that particles acquire mass by interacting with the Higgs field. This acquisition of mass occurs via spontaneous breaking of the underlying gauge invariant symmetries that make up the Standard Model framework.

The proposal of this Higgs field in the 1960s led to the consideration of a new scalar particle, the Higgs boson, formed from excitations of the field [1–3]. However, experimental evidence for the Higgs boson remained a significant missing component of the Standard Model for decades. Providing this evidence was one of the primary reasons for the construction of the Large Hadron Collider [4] (LHC) at the Conseil Européen pour la Recherche Nucléaire (CERN). The LHC is a proton-proton collider designed with a centre-of-mass energy of 14 TeV, built to test the experimental predictions of the Standard Model and look for New Physics in areas beyond the Standard Model. In 2012 the ATLAS and CMS collaborations, two separate general purpose particle detector experiments at the LHC, announced the observation of a new particle in the search for the Standard Model Higgs boson [5, 6].

Following on from the initial discovery, additional studies have been undertaken to probe this new particle and establish if it is consistent with the Standard Model Higgs boson. With these new studies and the increased experimental dataset provided by the continued running of the LHC; the spin, mass and couplings of the new particle have been shown to be consistent with the SM Higgs, and current measurements give the Higgs mass  $m_H = 125.09 \pm 0.29$  GeV [7].

There are several distinct production mechanisms proposed for a Higgs boson at the LHC. Of these mechanisms, the vector boson fusion (VBF) process is expected to have the second largest cross-section [8], and with a Higgs mass of  $\sim 125$  GeV, the dominant decay mode expected [9] is the  $H \rightarrow b\bar{b}$  mode. Measurement of the cross-section of VBF  $H \rightarrow b\bar{b}$  provides important information on the properties and behaviour of the Higgs boson, probing the strength of the VBF interaction and the coupling of the Higgs boson to down type quarks specifically. Analysis of the VBF  $H \rightarrow b\bar{b}$  has already been carried out by both the CMS [10] and ATLAS [11] collaborations on LHC proton-proton collision data at a centre-of-mass energy of 8 TeV. Studying this channel is complicated by the large background contributions from multijet events among other background sources, which necessitates limiting the trigger rate and reduces the number of relevant events.

At the LHC, the interaction rate far exceeds the possible data output rate, which is limited by the available bandwidth of the machine. As a result, the detector output relies on triggers to identify and record events of interest, which operate with pre-scaling reductions on event rates to reduce their output to within the bandwidth constraints. This results in significant numbers of discarded events for topologies lacking distinctive easy to detect signatures that can be used as a trigger. To overcome this limitation, the Trigger-Object Level Analysis strategy was proposed, where rather than storing the complete detector readout, the jet reconstruction information used in the triggering system is output and used for the physics analysis. This reduces the size of the detector output and allows the event output rate to be increased while remaining within bandwidth limitations. Such a TLA has been performed successfully, with a corresponding increase in rate, for the search for light dijet resonances at ATLAS [12].

The objective of this dissertation was to test the feasibility of applying a TLA to the search for the Higgs boson in the VBF  $H \rightarrow b\bar{b}$  channel. This was done by comparing the behaviour of trigger-level objects with standard analysis reconstructed objects, individually and with reference to the VBF  $H \rightarrow b\bar{b}$  topology. The analysis used  $4.6 \text{ fb}^{-1}$  of data taken during Run-2 of the LHC in 2016 at a centre-of-mass energy of 13 TeV.

An overview of the theoretical framework of the Standard Model and other physics relevant to the VBF  $H \rightarrow b\bar{b}$  interaction is given in Chapter 2. The experimental details of the ATLAS detector at the LHC are discussed in Chapter 3, while the specific details of the ATLAS data and analysis procedure for VBF  $H \rightarrow b\bar{b}$  are given in Chapter 4. Chapter 5 covers comparison of individual trigger-level objects to standard reconstructed objects and Chapter 6 contains similar comparisons with consideration of the overall VBF  $H \rightarrow b\bar{b}$  event. Finally, the conclusions of this dissertation are presented in Chapter 7.

# CHAPTER 2

## THEORY

### 2.1 Standard Model

The Standard Model (SM) of particle physics is a collection of several theories which provide the most accurate theoretical framework for describing all known components of matter and their interactions to date. The model describes three fundamental forces, each mediated by an integer spin particle called a *gauge boson*, that control interactions between the spin- $\frac{1}{2}$  *quarks* and *leptons* that make up matter. The mathematical structure is based on the symmetry group  $SU(3)_c \times SU(2)_L \times U(1)_\gamma$  and is required to be gauge-invariant. The Standard Model does not include gravity; gravity cannot currently be written in the Quantum Field Theories that describe the Standard Model, and gravitational interactions are significantly weaker than the other fundamental forces (Table 2.3). As a result, gravitational interactions are neglected hereafter.

#### 2.1.1 Fermions

The full set of spin- $\frac{1}{2}$  *fermions*, described in Tables 2.1 and 2.2, are the quark and lepton families, which each have three generations. For each distinct particle there is a paired *anti-particle* which is identical aside from opposite charges. The *handedness* or helicity of a particle refers to the projection of the angular momentum of the particle along the direction of the particle momentum. For a spin  $\frac{1}{2}$  particle, the angular momentum component can be aligned along the direction of motion (*positive* or *right-handed* alignment) or opposed to it (*negative* or *left-handed* alignment).

Most matter consists of the observable first generation of the up and down quarks and the electron which make up protons and neutrons, along with the electron neutrino. Both the leptons and the quarks obey Fermi-Dirac statistics. Quarks experience all three fundamental forces, charged leptons interacting via the electromagnetic and weak interactions and neutrinos experience only the weak interaction. Neutrinos have a special individual feature in that only left-handed neutrinos and right-handed anti-neutrinos have been observed. This asymmetry violates invariance under the *charge* (C) quantum operation and under the *parity* (P) operation individually, but does preserve CP invariance [13].

**Table 2.1:** Spin- $\frac{1}{2}$  fermions: quarks  $q$  [14].

Generation	Flavour	Charge / $e$	Mass / GeV
1	Up $u$	+2/3	$0.0022^{+0.0006}_{-0.0004}$
	Down $d$	-1/3	$0.0047^{+0.0005}_{-0.0004}$
2	Charm $c$	+2/3	$1.28 \pm 0.03$
	Strange $s$	-1/3	$0.096^{+0.008}_{-0.004}$
3	Top $t$	+2/3	$173.1 \pm 0.6$
	Bottom $b$	-1/3	$4.18^{+0.04}_{-0.03}$

**Table 2.2:** Spin- $\frac{1}{2}$  fermions: leptons  $l$  [14]

Generation	Flavour	Charge / $e$	Mass / MeV
1	Electron $e$	-1	$0.5109989461 \pm 0.0000000031$
	Electron Neutrino $\nu_e$	0	$< 2 \times 10^{-6}$
2	Muon $\mu$	-1	$105.6583745 \pm 0.0000024$
	Muon Neutrino $\nu_\mu$	0	$< 2 \times 10^{-6}$
3	Tau $\tau$	-1	$1776.86 \pm 0.12$
	Tau Neutrino $\nu_\tau$	0	$< 2 \times 10^{-6}$

Quarks are always confined into colour singlet *hadrons* bound by the strong interaction, which are either *baryons* ( $qqq$ ) like the *proton* ( $uud$ ) and *neutron* ( $ddu$ ), or *mesons* ( $q\bar{q}$ ) like the positive *pion* ( $u\bar{d}$ ).

### 2.1.2 Forces

All forces arise due to the exchange of integer spin particles, gauge bosons, which obey Bose-Einstein statistics. The three fundamental particle interactive forces for the Standard Model are named the strong, weak and electromagnetic interactions, and are mediated by *gluons*, *weak bosons* and *photons* respectively. The gauge bosons are described in more detail in Table 2.3.

**Table 2.3:** Spin-1 gauge bosons. The strength of the interaction is typically stated in terms of  $\alpha$ , a dimensionless constant proportional to the matrix element for the virtual particle exchange for each interaction. The weak interaction is intrinsically stronger than the EM interaction, but the mass of the weak bosons limits the range to extremely short distances. The strength of gravity is  $\sim 10^{-39}$  hence it is neglected. [14]

Interaction	Particle	Charge / $e$	Mass / GeV	Strength ( $\alpha$ )
Strong	Gluon $g$	0	0	$\sim 1$
Weak (Charged Current)	$W^+$	1	$80.385 \pm 0.015$	$10^{-6}$
	$W^-$	-1	$80.385 \pm 0.015$	
Weak (Neutral Current)	$Z$	0	$91.1876 \pm 0.0021$	
Electromagnetic (EM)	Photon $\gamma$	$< 1 \times 10^{-35}$	$< 1 \times 10^{-27}$	$\frac{1}{137}$

Along with gauge bosons acting as force carriers for interactions, most gauge bosons have a degree of self-coupling which leads to self-interactions. The gluon couples with particles that contain-colour charge, but as the gluon itself possesses a colour charge, gluons may interact with other gluons in exchange processes similar to the exchange of a force carrier between two interacting particles. This self-interacting behaviour is also seen in the  $W$  and  $Z$  bosons as they couple to the weak charge they carry, but no self-interactions are observed for the photon as it does not carry electromagnetic charge [13].

#### 2.1.2.1 Quantum Chromodynamics

Quantum Chromodynamics (QCD) is the theory of the strong interaction mediated by the gluon which couples to colour charge. It corresponds to the  $SU(3)_c$  symmetry group of the overall Standard Model. The strong interaction conserves energy, momentum, angular momentum and colour charge. Only quarks and gluons themselves possess colour charge, so quarks are the only fermions to feel the strong interaction. As highlighted above, this also means gluons are capable of self interaction, which leads to two distinct properties of the string interaction: *colour confinement* and *asymptotic freedom*.

Colour confinement is the requirement that observable states have net zero colour charge. This means gluons, like quarks, are only observed in bound states. Asymptotic freedom de-



scribes how the interaction gets weaker at short distances, and means that at close distances, such as quark-quark scattering, the interaction normally proceeds through a lowest-order single gluon exchange interaction. The converse of this is that the force increases significantly as the interaction distance increases and higher-order Feynmann interaction diagrams become significant [13].

### 2.1.2.2 Electroweak Unification

Electroweak Unification (EW) is the expression of the electromagnetic interaction and the weak interaction as separate manifestations of a combined electroweak force in the Glashow-Weinberg-Salam model [15–17], which corresponds to the  $SU(2)_L \times U(1)_Y$  symmetry group. Quantum Electrodynamics (QED) describes the macroscopically observable  $U(1)$  electromagnetic force with the photon as the mediating boson, and any interaction conserves energy, momentum, parity and charge and, additionally, never changes particle type through the interaction. The  $SU(2)$  weak interaction is mediated by the charged current vector bosons  $W^+$ ,  $W^-$  and the neutral current vector boson  $Z$ , which have large masses that limit the weak interaction to very short distances. The charged current interaction is capable of changing the flavour of a particle and also of violating parity in an interaction.

The weak interaction by itself was observed to diverge from observation at high energies, leading to the introduction of the unified theory. The combined  $SU(2)_L \times U(1)_Y$  group produces four gauge bosons which mix to produce the more recognisable  $\gamma$ ,  $W^+$ ,  $W^-$  and  $Z$  bosons. This weak interaction couples to weak isospin charge, which is an analogous quantity to the colour charge of QCD. As the weak bosons carry weak isospin charge themselves, self coupling of the weak bosons is permitted, but is forbidden for the photon as it does not carry electric charge. The weak interaction has been experimentally observed to violate parity conservation [13, 18].

While the weak interaction acts on both quarks and leptons, weak interaction in the quark sector is affected by *quark mixing*. In this construction, the quark mass eigenstates  $q$  participate in weak interactions via the weak eigenstates  $q'$  formed from linear combinations of the  $q$  states [13]. The observable result of this quark mixing is that different flavour changing interactions have different strengths.

The coupling relationships of the weak and mass eigenstates is described by the unitary Cabbibo-Kobayashi-Makasawa matrix  $V_{CKM}$  [19, 20]

$$\begin{pmatrix} d' \\ s' \\ b' \end{pmatrix} = \begin{pmatrix} V_{ud} & V_{us} & V_{ub} \\ V_{cd} & V_{cs} & V_{cb} \\ V_{td} & V_{ts} & V_{tb} \end{pmatrix} \begin{pmatrix} d \\ s \\ b \end{pmatrix}, \quad (2.1)$$

shown here transforming between the two sets of eigenstates  $q$  and  $q'$ . The CKM matrix elements  $V_\alpha$  of  $V_{CKM}$  describe the relative couplings of the eigenstates, and are parametrised in terms of three mixing angles and one complex phase [20, 21].

### 2.1.3 Spontaneous Symmetry Breaking: The Higgs Boson

The gauge field theories used for the QCD and EW models when unaltered require massless gauge bosons to preserve gauge invariance. This is satisfactory for the gluon and photon, but a separate theory is required to explain the mass of the  $W^\pm$  and  $Z$  bosons. The *Higgs mechanism* proposed a method for particles to acquire mass by coupling to the spin-0 *Higgs* field via the Higgs boson [1–3]. This process as proposed is an example of a *spontaneous symmetry breaking* process, where the gauge invariance of the interaction is preserved but the ground state breaks the invariance.

The Higgs Mechanism introduces a complex doublet of scalar fields  $\phi$  that interact with the  $W^\pm$  and  $Z$  fields. In the Lagrangian formulation this results in a term akin to a mass term ( $\propto \psi^2$ ) which effectively links that mass of the bosons to their coupling with this scalar field. This field self-interacts to produce a potential energy  $V(\phi)$  given by

$$V(\phi) = \mu^2 \phi^2 + \lambda \phi^4, \quad (2.2)$$

resulting in an equilibrium point ( $\phi = 0$ ) that respects the symmetry but is inherently unstable, with an infinite set of degenerate non-zero minima. This minima, the lowest energy level vacuum state, occurs at  $|\phi^2| = v^2 = \frac{-\mu^2}{2\lambda}$  where the symmetry is *spontaneously* broken. This field, in an analogous fashion to the other quantum fields of the Standard Model, can produce particles from excitations which form the physical *Higgs Scalar Boson H*.

Confirmation of the Higgs boson as part of the Standard Model was only achieved relatively recently [22, 23], where a spin-0 boson consistent with the Standard Model Higgs boson was observed by the ATLAS and CMS experiments at the LHC. Section 2.3 covers in more detail the production and behaviour of the Higgs boson in collider experiments.

## 2.2 Physics of $pp$ Collisions

### 2.2.1 $pp$ Collisions

Recent experimental efforts to probe the Standard Model have focused on high-energy collider experiments, where beams of particles with equal energy are collided head on within detector volumes. For proton-proton ( $pp$ ) collisions, matters are complicated as the colliding protons are composite particles, which at high energy consist of the three *valence* quarks and a sea of virtual quarks and gluons. Collectively these constituents are referred to as *partons*, where each parton carries a fraction of the overall hadron momentum, and the interaction in the  $pp$  collision consists of elastic scattering between these partons. At a given energy scale  $Q^2$ , the probability that a parton  $i$  carries a fraction  $x_i$  of the overall momentum is described by the parton distribution function (PDF)  $f_i(x, Q^2)$ . These PDFs cannot be calculated from QCD but can be determined from experimental measurements, and collections of PDFs have been assembled from the leading collider experiments [24,25].

In any particle interaction, the probability of a particular reaction occurring is in proportion to the cross-section of the reaction. The cross-section for a short range, hard parton-parton collision is given by  $\hat{\sigma}(Q^2)$ , where scattering energy scale  $Q^2 = x_1 x_2 E_{cm}^2$  in the parton-parton centre-of-mass frame where  $E_{cm}$  is the energy in the centre-of-mass frame. To compute the cross-section  $\sigma$  for some hard process  $pp \rightarrow X$ , all possible combinations of incoming partons must be summed over and the momentum fractions integrated over while accounting for the PDFs,

$$\sigma_{pp \rightarrow X} = \sum_{i,j} \int dx_1 dx_2 f_i(x_1, Q^2) f_j(x_2, Q^2) \hat{\sigma}_{ij \rightarrow X}(Q^2), \quad (2.3)$$

where as above  $x_i$  are the momentum fractions and  $f_i$  the PDFs [24]. The PDFs used in these calculations contain series expansion terms, which as a construction is referred to as perturbation theory. This allows truncation of the series expansion to the first few terms, which starts with using just a single term for leading-order (LO) calculations, adding a second for next-to-leading-order (NLO) and continues onwards beyond next-to-next-to-leading-order (NNLO) [24].

### 2.2.2 Geometry

The high energy protons used in collisions are relativistic in nature, and as the momenta of the colliding partons are not in general equal and opposing there is always an unknown longitudinal boosting in  $pp$  collisions. As a consequence, use of light-cone coordinates and definition of some convenient quantities can be of benefit to  $pp$  collision analyses [26].

Typically the particle kinematics are defined by transverse momentum  $p_T$  and rapidity  $y$ . Rapidity is defined by

$$y = \frac{1}{2} \ln \frac{E + p_z}{E - p_z}, \quad (2.4)$$

where  $E$  is the energy of a particle and  $p_z$  is the momentum component along the beam axis  $z$ . This rapidity  $y$  transforms additively to boosts along the  $z$  axis, so any rapidity difference between two objects is invariant to such boosts. For cases where the mass of a particle is negligible (highly relativistic particles) the rapidity can be approximated by the pseudo-rapidity  $\eta$ , defined as

$$\eta = -\ln \tan \frac{\theta}{2}, \quad (2.5)$$

where  $\theta$  is the polar angle. The distance between two objects within the detector is commonly expressed in the  $(\eta, \phi)$  space rather than absolute, with this separation being given by  $\Delta R = \sqrt{(\Delta\eta)^2 + (\Delta\phi)^2}$ .

### 2.2.3 $pp$ Event Simulations

A  $pp$  collision is a complex event which results in a significant number ( $O(1000)$ ) of final state particles, each of which interact and evolve over the timescale of an event. This progression of the collision event can be broken down into distinct stages of behaviour of the produced particles: the *hard process*, *parton shower*, *hadronisation*, *unstable particle decays* and *underlying event* [27].

This breakdown is key to the simulation of  $pp$  collisions using Monte-Carlo event generators, the use of which is critical in current high energy physics research. Monte-Carlo simulations of collisions are used to predict and prepare for real data-taking experiments, obtain control datasets of particular particle interactions and act as controls to optimise analysis tools. The breakdown of the interaction into distinct stages has allowed specialised software to be produced for each step, which makes use of a characteristic scale and certain safe approximations for the step to provide reliable predictions, while reducing the computational demands of the simulation [27].

There is a broad selection of software tools for evaluating  $pp$  collisions, from general purpose simulations like PYTHIA [28] or SHERPA [29] which are used to evaluate the complete process, to more specific tools like POWHEG [30] which is used to produce hard scatter events with NLO matrix elements. Most software packages make use of the chain of generation for an event outlined previously, and modern analyses will make use of multiple generators interfaced together to compute different steps with improved accuracy.

### 2.2.3.1 Hard Process

The first stage of a  $pp$  collision and the first step of a simulation, the hard scatter refers to highest momentum transfer process in the event between coloured particles, and forms the core of the event. This details the interaction of partons entering the event and those outgoing particles resulting from the process. In simulation the probability distribution of the partons is calculated from perturbation theory to the desired accuracy (LO, NLO etc) using the PDFs of the constituents as covered by equation 2.3 in Section 2.2.1.

### 2.2.3.2 Parton Shower

While the hard scatter interaction in a collision is relatively straightforward, the overall behaviour of the partons is much more complex as they progress through the event. The incoming and outgoing partons from the hard scatter radiate additional particles during the event [13, 27]. The Bremsstrahlung radiation of photons by scattered electric charges is well described by QED, and the analogous radiation of gluons by scattered colour charges as explained by QCD produces additional partons within the interaction. However, as the gluons produced by QCD scattering themselves carry colour charge, there is extensive showering of gluons producing gluons, resulting in the phase space of the interaction being filled with a sea of soft gluons. In addition to the self interactions, quark and gluon processes,  $g \rightarrow q\bar{q}$  and  $q \rightarrow g\bar{g}$ , occur. These radiative processes make up the parton shower stage of the event simulation [27].

The evolution of these parton showers is evaluated in Monte-Carlo simulations using a step-by-step iterative process, on the scale of momentum transfer in the interaction. This process is started at the hard scatter and evolved through the interaction with decreasing momentum scale until the point at which perturbation theory breaks down, necessitating a different evaluation method [27].

### 2.2.3.3 Hadronisation

The breakdown of perturbation theory at low momentum scales implies the strong force coupling is very large, and observable colourless hadrons are formed from the coloured partons using hadronisation models in order to extend the simulation. These hadrons are the physical final state particles observed in the detector, which exist due to the colour confinement of the quarks and gluons. Within a particle detector collimated *jets* of hadrons are observed rather than individual hadrons. The parton shower process produces large numbers of gluons and quarks moving out in a collimated stream from the interaction.

Partons and gluons are not the final state particles and cannot propagate freely, so at this point hadronisation occurs to collect the partons into the final state particles [27].

In simulation this step involves collecting the partons produced in the parton shower into hadrons, and is typically evaluated using either a String model [31] or a Cluster model [27,32]. These steps are models, and not calculations as to how the partons combine, as such calculations are prohibited by the breakdown of perturbation theory. The models themselves were produced by tuning the simulations to data from past experiments like the Large Electron-Positron collider previously operational at CERN, and current data from the LHC [33,34].

#### 2.2.3.4 Unstable Particle Decays

The final stage of the evolution of the parton shower considers the hadrons produced during the shower. These hadrons may not be stable particles but could be resonances that go on to decay within the detector to produce the more stable hadrons observed in the data. Most modern simulation software models these decays, but the exact specification of the decay tables and channels has a significant impact on the final state of the simulation [27].

#### 2.2.3.5 Underlying Event

While the hard scatter and subsequent parton shower results from the highest momentum interaction of the  $pp$  collision, the remnants of the proton not involved in this will continue to interact with each other. This produces additional soft hadrons that fill the interaction environment, overlapping with the products of the hard scatter interaction.

The dominant model for simulation of the underlying event is a perturbative model, where the other components of the event undergo additional discrete hard scatter interactions and corresponding parton showers, which are simulated in an corresponding fashion to the core scattering.

## 2.3 The Higgs Boson

Detecting the Standard Model Higgs boson is strongly dependent on the predominant production and decay channels for the Higgs boson. In this section, the relevant production and decay channels at the Large Hadron Collider (LHC) will be discussed.

### 2.3.1 Higgs Production

While there are various methods for production of a Higgs boson, at the LHC the cross section is dominated by gluon-gluon fusion ( $gg \rightarrow H$ ) as shown in Figure 2.2, with the second largest cross-section arising from Vector Boson Fusion (VBF, Section 2.3.4). Other significant production processes are the associated production with a weak boson ( $WH/ZH$ , Higgs-Strahlung) and associated production with top quarks ( $t\bar{t}H$ ) [8]. The lowest order Feynmann diagrams for these processes are shown in Figure 2.1.

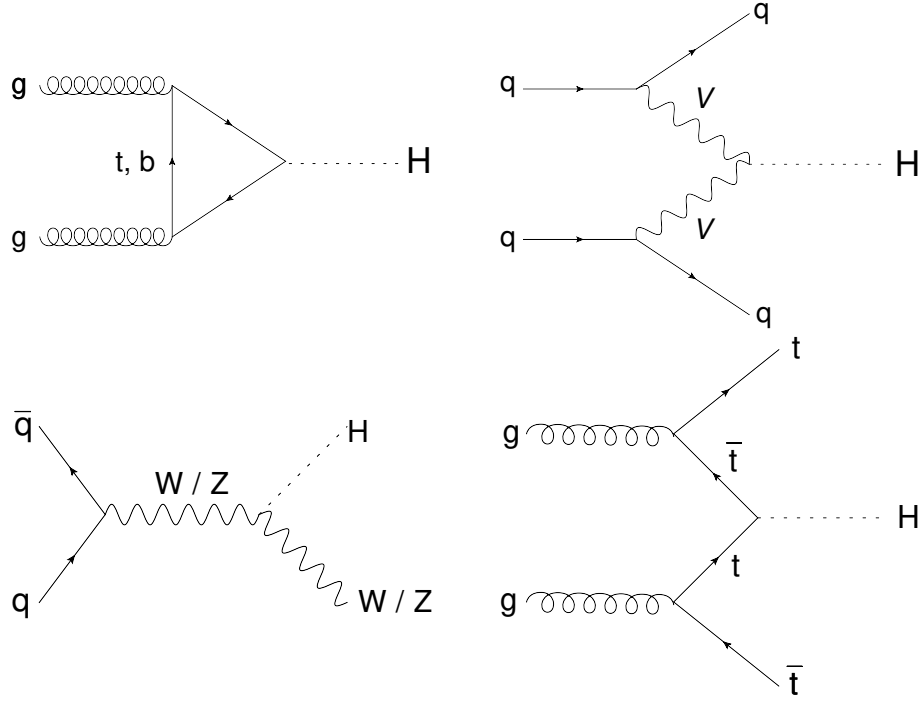


**Figure 2.1:** Lowest order Feynmann diagrams for gluon-gluon fusion ( $gg \rightarrow H$ ), vector boson fusion (VBF),  $W/Z$  associated production ( $WH/ZH$  or  $VH$ ) and top anti-top associated production ( $t\bar{t}H$ ) [35].

The dominant production mechanism for the Higgs boson in hadron colliders is the  $gg \rightarrow H$  production via an intermediate quark loop [35]. The dynamics of this mechanism are controlled by strong interactions, thus calculations of QCD corrections are necessary for accurate predictions, and have been computed up from next-to-leading order (NLO) to  $N^3\text{LO}$  for the  $gg \rightarrow H$  process in recent years, along with the inclusion of Electro-Weak corrections in the cross-section calculations [8]. The production has a cross-section that is between one and two orders of magnitude larger than the other production channels as shown in Figure 2.2. The second largest cross section is that for vector boson fusion, which has a well defined experimental signature due to the two remnant jets produced along with the Higgs boson, and has a well defined NLO cross-section with small QCD corrections [36].

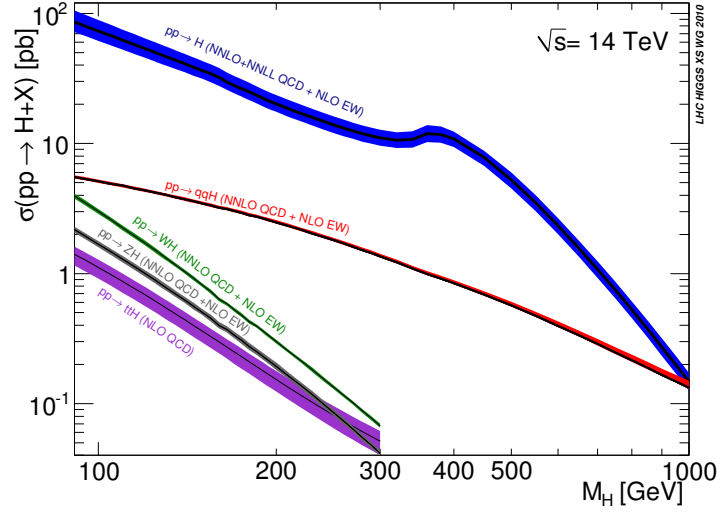


**Figure 2.2:** SM Higgs production cross section for  $\sqrt{s} = 14$  TeV.  $pp \rightarrow H$  corresponds to gluon-gluon fusion production,  $pp \rightarrow qqH$  vector boson fusion,  $pp \rightarrow WH$  and  $pp \rightarrow ZH$  to  $W/Z$  associated production and  $pp \rightarrow ttH$  refers to top anti-top associated production [8].

The two other principal production modes at the LHC, the Higgs-strahlung associated  $W/Z$  production and associated production with a top quark pair, have very small cross-sections compared to the  $gg \rightarrow H$  and VBF production modes. While Higgs searches for these channels must work around the small event rate by using final states with a clear signature, analysis of these channels is possible [37, 38].

### 2.3.2 Higgs Decay

The branching ratios for decays of the Higgs boson in the Standard Model have been calculated according to the theoretical framework of the Standard Model [9]. The branching ratios for the decays of the Higgs boson are shown in Table 2.4.

At a Higgs mass of  $\sim 125$  GeV the dominant decay mode, shown in Table 2.4, is the  $H \rightarrow b\bar{b}$  mode. While this is the dominant decay mode at this Higgs mass, Higgs searches will make use of other decay channels where the final state signature is clearer and easier to trigger events on, such as the leptonic decays  $H \rightarrow \tau\tau$  and  $H \rightarrow \gamma\gamma$ . Higgs decays to gauge bosons also offer clear final states as they will subsequently decay to leptons [40, 41].

At the LHC, the two main search channels for the Higgs boson are the  $H \rightarrow ZZ^* \rightarrow 4l$  and  $H \rightarrow \gamma\gamma$  channels [40, 42], with the main search channel for  $H \rightarrow b\bar{b}$  being the Higgs-Strahlung VH production with subsequent  $H \rightarrow b\bar{b}$  and the vector boson  $V$  ( $V = W, Z$ ) decaying  $V \rightarrow l + X$ . The other principal production modes and alternative decay channels



**Table 2.4:** Branching ratios and uncertainties of a Standard Model Higgs boson with  $m_H = 125$  GeV [39].

Decay	Branching ratio	Relative Uncertainty
$H \rightarrow b\bar{b}$	$5.84 \times 10^{-1}$	+3.2% -3.3%
$H \rightarrow W^+W^-$	$2.14 \times 10^{-1}$	+4.3% -4.2%
$H \rightarrow \tau^+\tau^-$	$6.27 \times 10^{-2}$	+5.7% -5.7%
$H \rightarrow ZZ$	$2.62 \times 10^{-2}$	+4.3% -4.1%
$H \rightarrow \gamma\gamma$	$2.27 \times 10^{-3}$	+5.0% -4.9%
$H \rightarrow Z\gamma$	$1.53 \times 10^{-3}$	+9.0% -8.9%
$H \rightarrow \mu^+\mu^-$	$2.18 \times 10^{-4}$	+6.0% -5.9%

are also used in searches for the Higgs boson however. Searches in the  $t\bar{t}H$  channel make use of  $W$  bosons from  $t$  quarks decaying into zero, one or two leptons [43], and vector boson fusion can exploit the distinctive final state signature. Discussion of VBF searches, specifically VBF  $H \rightarrow b\bar{b}$ , are given in Section 2.3.4.

### 2.3.3 Summary of Current Higgs Measurements

As of early 2018, the LHC has delivered more than  $40 \text{ fb}^{-1}$  of 13 TeV  $pp$  collisions to the ATLAS and CMS detectors (Section 3.1), and Higgs searches have been carried out in wide variety of decay channels ( $WW$ ,  $BB$ ,  $\gamma\gamma$ ) and production modes ( $gg \rightarrow H$ , VH, VBF) [11, 39, 43, 44]. The consensus of these analyses is that the CMS and ATLAS experiments have observed the Standard Model Higgs boson with a mass of  $125.09 \pm 0.24$  GeV [14].

### 2.3.4 Searches for VBF $H \rightarrow b\bar{b}$

Production of a Higgs boson from the fusion of vector bosons radiated from initial-state quarks is the second largest cross-section at the LHC, and is useful as a production mode due to topological characteristics which can distinguish the event from  $gg \rightarrow H$ . In VBF  $H \rightarrow b\bar{b}$ , the characteristic topology is a pair of central  $b$ -jets forming the Higgs candidate, and two forward, close to the beam line VBF jets formed from remnants of the initially colliding protons as displayed in Figure 2.1. In addition, central jet activity is suppressed due to the lack of colour exchange between the colour singlet Higgs boson and the decay  $b$ -quarks [45]. These distinctive features mean that VBF can be distinguished from the other production mechanisms and from the main background processes.

Searches for the VBF  $H \rightarrow b\bar{b}$  interaction look for a resonance in the invariant mass of a pair of jets containing  $b$ -quarks( $m_{bb}$ ) in events with the characteristic topology. This characteristic topology distinguishes the signal events from the multijet events that form the dominant background with a non-resonant  $m_{bb}$  spectrum. An additional resonant background contribution to the  $m_{bb}$  spectrum is due to decay of a  $Z$  boson to two jets in association with two jets. With the application of specific cuts to take advantage of this topology, the VBF channel provides a clean environment for analysis [39].

In the most recent searches for the Higgs boson produced via VBF, which this analysis emulates [11], the VBF  $H \rightarrow b\bar{b}$  events are separated from non-Higgs backgrounds using a multivariate boosted decision tree (BDT) analysis (Appendix B) to refine the phase space to the most VBF sensitive BDT regions.

## DETECTOR

### 3.1 The Large Hadron Collider

The LHC is a circular particle accelerator operated at CERN. Currently the largest accelerator in the world, the LHC is designed to collide opposing beams of protons at a *centre-of-mass* energy  $\sqrt{s} = 14$  TeV and a peak *luminosity* of  $10^{34} \text{ cm}^{-2}\text{s}^{-1}$  [4]. The first proton beams were circulated in the LHC in 2008, with Run-1 of LHC data taking being conducted from 2010 to 2012 at increasing  $\sqrt{s}$  of 7 and 8 TeV, after which the machine was shut down for scheduled maintenance. Following on from the long shut down period, Run-2 of the LHC has been ongoing since 2015, operating at  $\sqrt{s} = 13$  TeV.

The principal LHC ring consists of eight pairs of alternating long arc sections and short straight insertion sections, situated within the underground tunnel excavated for the older Large Electron Positron Collider experiment [46,47]. The arc sections contain the dipole magnets used to bend the particle beam around the ring, while the straight sections contain four interaction points, at each of which the large experiments are located. The remaining straight sections contain the operational systems of the LHC: beam acceleration, injection, dumping and collimation. The proton beams are generated outside the principal ring and inserted into the ring by the LHC injector chain, a sequence of smaller accelerators which are used to bring the proton beams up to a suitable energy for injection. The proton beams injected into the accelerator are obtained from a cloud of hydrogen gas, which is passed through an electric field to strip the electrons before the protons are inserted into the beam acceleration components. The proton beams are arranged such that the protons move in

bunches of  $O(10^{11})$  protons, with multiple bunches placed into trains. During Run-2 the LHC operated with bunch spacings of 50 ns and 25 ns.

A key operational parameter of any accelerator is the instantaneous beam luminosity  $L$ . This parameter is a measure of the rate of collisions within the accelerator, given by

$$L = \frac{1}{\sigma} \frac{dN}{dt} = \frac{n_b n_1 n_2 f}{2\pi \Sigma_x \Sigma_y}, \quad (3.1)$$

where in the general case  $\sigma$  is the interaction cross section,  $\frac{dN}{dt}$  is the event rate,  $n_b$ ,  $n_1$  and  $n_2$  are the number of bunches, and the number of particles per bunch in both of the colliding beams,  $f$  the machine revolution frequency, and  $\Sigma_{x,y}$  are parameters relating to the beam width. This instantaneous luminosity is integrated across a time period, such as an LHC Run or a specific data period, to produce the integrated luminosity  $\int L dt$  which is a measure of the total recorded data.

Once a beam is accelerated to the target energy, collisions begin at the interaction points. Interactions are ongoing for periods of several hours, and will continue until the the beam is replaced due to general decay of the interaction rate or beam instabilities occur.

At the LHC, the four large experiments at the interaction points are ATLAS [48](A Toroidal LHC ApparatuS), CMS [49](Compact Muon Solenoid), LHCb [50](LHC beauty) and ALICE [51](A Large Ion Collider Experiment). LHCb is a forward spectrometer heavy flavour experiment, designed to study flavour physics with emphasis on  $b$ -quarks,  $c$ -quarks and on matter/anti-matter asymmetry. ALICE focuses on the collisions of heavy ions, while ATLAS and CMS are general purpose detectors to conduct experiments across a broad range of modern physics research areas.

### 3.1.1 LHC Run Conditions in 2016

Over the course of 2016, following beam commissioning runs, the LHC beam was operated predominantly with two beams of energy 6.5 TeV for  $\sqrt{s} = 13$  TeV. Over the course of the 2016 data-taking the LHC provided an integrated luminosity of  $\sim 40 \text{ fb}^{-1}$  to the ATLAS and CMS experiments with a peak instantaneous luminosity of  $1.4 \times 10^{34} \text{ cm}^{-2}\text{s}^{-1}$  with 2220 bunches per beam [52].

## 3.2 The ATLAS Detector

The ATLAS detector [48] is a multi-purpose detector designed to study a broad selection of physics phenomena within the experimental conditions of the LHC. The detector is cylindrical in structure with the axis aligned to the beam path and nominally forward-backward symmetric in terms of the beam collision point at the centre of the detector. The detector provides approximately  $4\pi$  solid angle coverage around the interaction point to detect as many collision products as possible.

The structure of the ATLAS detector is composed of concentric subsystems around the interaction point. The Inner Detector (ID) is the component closest to the interaction point, and is contained in a superconducting solenoid. This is surrounded by high-granularity calorimeters and an extensive muon spectrometer contained within an eight-fold azimuthally symmetric arrangement of three large toroidal magnets. A schematic representation of the ATLAS detector is shown in Figure 3.1. The detector consists of three main sections, two *endcaps* located on the ends of the detector and a central *barrel* section. A summary of the operational parameters of the principle detector components is given in Table 3.1.

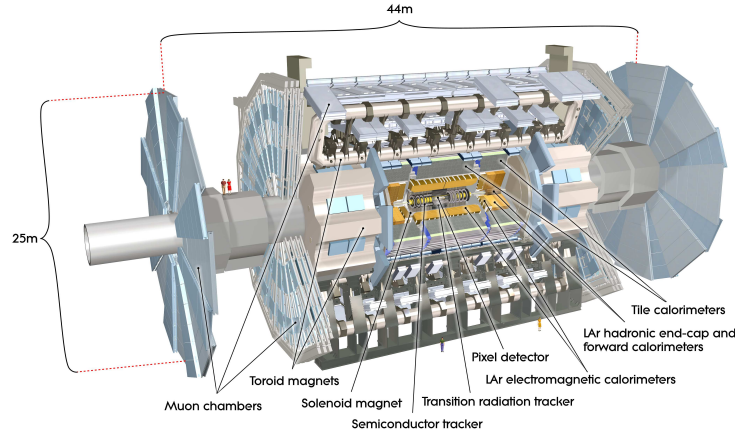


**Figure 3.1:** Schematic cut-away of the ATLAS detector [53].

The conventional coordinate system used to describe the detector takes the interaction point as the origin, with  $x$  pointing horizontally out into the centre of the detector ring,  $y$  out and upwards with  $z$  along the direction of the beam line. The angle  $\phi$  describes azimuthal rotation around the beam pipe and  $\theta$  is the polar angle along the beam line.

### 3.2.1 Inner Detector

The Inner Detector [54] (ID) provides pattern recognition, momentum measurements, electron identification and measurements of both primary and secondary vertices to efficiently

identify  $b$ -hadron decays within a pseudorapidity range  $|\eta| < 2.5$ . The ID itself is contained within a 2 T solenoidal field, which is used to bend the paths of charged particles within the ID. The ID is specifically designed to have a good momentum resolution (Table 3.1), and consists of three separate detector sections: the silicon pixel detector provides fine granularity track and vertex reconstruction, the silicon strip semiconductor tracker measures the trajectory of transiting charged particles and the outer transition radiation tracker used for particle identification is comprised of layers of straw tubes containing mixtures of xenon, oxygen and carbon dioxide [48].

### 3.2.2 Calorimeters

Calorimeters are used to measure the energy of interacting particles moving out from the interaction point. These particles cause the development of energy showers within the calorimeter substrate, forming different shower types depending on the interaction force of the particle, with electromagnetic (EM) showers forming from EM interactions and hadronic showers forming from interactions via the strong nuclear force. The energy deposited in this shower can be then used to calculate the energy of the incoming particle. The ATLAS calorimetry system consists of a combination of EM and hadronic calorimeters arranged with full  $\phi$ -symmetry around the beam axis. The combination of all separate calorimeters provides pseudorapidity coverage in the range  $|\eta| < 4.9$ . Within the pseudorapidity region of the inner detector, the fine granularity of EM calorimeters is optimised for measurements of electron and photons, while the coarser hadronic calorimeters contained in the remainder of the calorimeter system are sufficient for measurements of the energy of produced hadrons. The structure and design of the calorimeter components has been optimised to provide complete azimuthal coverage, taking into account the engineering requirements for assembling the detector and providing sufficient radiation hardness along with a sufficiently hermetic interaction environment [48].

The EM calorimeter [55] is a lead-Liquid-Argon (LAr) detector, which is split into a barrel section (EMB,  $|\eta| < 1.475$ ) and two endcap sections (EMEC,  $1.375 < |\eta| < 3.2$ ) with each section contained in a separate cryostat. The EMB consists of two identical half-barrels split by a small gap at  $z = 0$ . Each of the EMEC sections is a pair of coaxial wheels, with the inner and outer sections covering regions  $1.375 < |\eta| < 2.5$  and  $2.5 < |\eta| < 3.2$  respectively. The major body of the EM calorimeter is divided into three sections of decreasing cell granularity, moving out from the beamline.

Hadronic calorimetry for particles undergoing the strong interaction is provided by the steel/scintillator tile calorimeter [56] for pseudorapidity values of  $|\eta| < 1.7$ , and by the LAr flat-plate Hadronic Endcap Calorimeter (HEC) for  $1.5 < |\eta| < 3.2$ . The tile calorimeter

directly surrounds the EM calorimeter, and is split into a central barrel section for  $|\eta| < 1.0$  and two extended barrel sections covering  $0.8 < |\eta| < 1.7$ . The HEC, akin to the EMEC, consists of two separate wheels per end-cap covering  $1.5 < |\eta| < 3.2$ , and is contained within the same cryostat as the EMEC. The HEC consists of alternating copper plates with LAr gaps to act as the active medium.

In addition to the barrel and end-cap calorimeters, the LAr Forward Calorimeter [57] is contained within the end-cap cryostat (The FCal is omitted from Figure 3.1) and is designed to perform both EM and hadronic calorimetry across a pseudorapidity range of  $3.1 < |\eta| < 4.9$  using a combination of copper/LAr (EM) and tungsten/LAr (hadronic) calorimeter components.

### 3.2.3 Muon Spectrometer

The muon spectrometer is the outermost component of the ATLAS detector, measuring trajectory and momentum of muons within a pseudorapidity range of  $|\eta| < 2.7$ . The muon system consists of three large superconducting coils that deflect the muon trajectories and a suite of tracking devices. The system is designed for high precision tracking of the muons and for use in the triggering system of the overall detector. The triggering chambers consist of Resistive Plate Chambers and Thin Gap Chambers which can respond to a particle transit in  $O(10)$  ns, while the precision momentum measurement is carried out in Monitored Drift Tubes and Cathode Strip Chambers arranged in layers [48].

**Table 3.1:** Performance goals and operational ranges for the principal components of the ATLAS detector, given in terms of energy  $E$ , transverse momentum  $p_T$  and corresponding resolutions  $\sigma_E/E$  and  $\sigma_{p_T}/p_T$ . [48]

System	Component	$\eta$ Coverage	Resolution
Tracking		$0 <  \eta  < 2.5$	$\sigma_{p_T}/p_T = 0.05\% p_T \oplus 1\%$
EM Calorimetry	EMB	$0 <  \eta  < 1.475$	$\sigma_E/E = 10\%/\sqrt{E} \oplus 0.7\%$
	EMEC (Inner)	$1.375 <  \eta  < 2.5$	
	EMEC (Outer)	$2.5 <  \eta  < 3.2$	
Hadronic Calorimetry	Tile (Barrel)	$0 <  \eta  < 1$	$\sigma_E/E = 50\%/\sqrt{E} \oplus 3\%$
	Tile (Extended)	$0.8 <  \eta  < 1.7$	
	HEC	$1.5 <  \eta  < 3.2$	
Forward Calorimetry	FCal	$3.1 <  \eta  < 4.9$	$\sigma_E/E = 100\%/\sqrt{E} \oplus 10\%$
Muon Spectrometer		$0 <  \eta  < 2.7$	$\sigma_{p_T}/p_T = 10\% \text{ at } p_T = 1 \text{ TeV}$

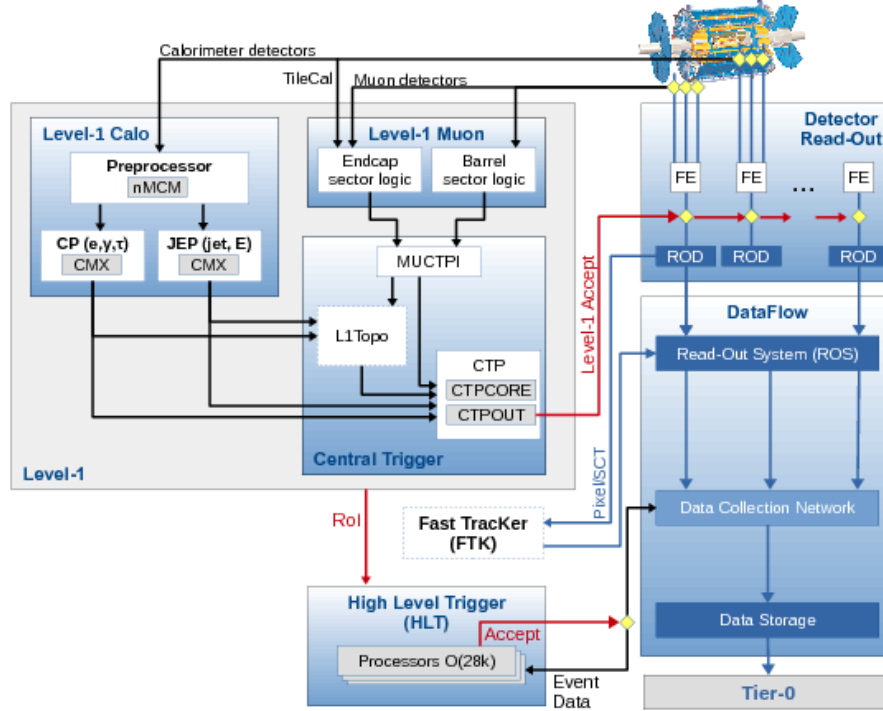


Figure 3.2: Schematic plot of the ATLAS Trigger and Data acquisition system [59].

### 3.3 Trigger and Data Acquisition

When operating at the design luminosity, the LHC produces a bunch-crossing rate of 40 MHz [58]. This rate of interaction necessitates a trigger system to reduce the output rate to a suitable level for offline processing, which is predominantly limited by the rate at which data can be written to disk. The trigger system selects events by quickly identifying distinguishing features of events, signatures of muons, electrons, jets and  $b$ -jets, and using combinations of these signatures to signify an event as relevant for further analysis.

The ATLAS trigger system consists of a chain of selection stages of increasing complexity and corresponding decrease in rate. A schematic outline covering both the logical process and the transfer of data between components of the trigger chain is shown in Figure 3.2. The principal decision logic of the trigger system is contained in two sections, the Level 1 (L1) trigger system and the High Level Trigger (HLT).

The L1 trigger system [60] is a hardware-based decision system, using fast custom electronics to minimise latency in any decision. The L1 uses reduced-granularity data from the calorimetric and muon detectors, reconstructed objects and missing and total transverse energy. The high bunch-crossing rate means instantaneous processing of the event is non-



viable, so event readouts are stored in a buffer chain of events to be evaluated with a fixed permitted decision time per event. Along with this first selection, the L1 trigger defines *Regions of Interest* (RoIs) in the phase space within the detector, which are labeled for investigation in the HLT.

In contrast to the hardware computation of the L1 system, the HLT consists of software algorithms running in a farm of  $\approx 40000$  interconnected processors [58]. Following acceptance of an event by the L1 trigger, events are transferred from the initial data pipeline to dedicated readout buffers for the HLT. The HLT performs processing on the events using finer-granularity information from the calorimeters and muon spectrometer, along with making use of information from the ID, which is unavailable to L1. This more precise data is then computed using object reconstruction algorithms to generate particle objects similar to the objects reconstructed using the full output of the detector. The decision at HLT level to store an event is managed by a trigger chain, which is a sequence of specific criteria and algorithms evaluated on an event in sequence.

A key component of the trigger chain is the prescaling factor of the chain, where the overall output rate of the trigger chain is reduced by the prescale factor to bring the output rate within bandwidth limits. The trigger menu in 2016 provided a selection of main ATLAS triggers used for the data-taking [61], with large numbers of distinct independent HLT trigger chains for evaluating events. Along with the partial reconstruction of relevant objects, the HLT is capable of performing complete reconstruction of an event, and also capable of writing out these partial or complete reconstructions of an event into different data streams from the complete detector readout for use in analysis. The standard terminology for events and data recorded and processed during the operation of the LHC is *online* data, while objects and information produced by considering the output of the detector after the data has been stored is termed *offline*. These terms are used extensively throughout the rest of this dissertation to distinguish between the different data sources.

Overall usage of the trigger system brings the output rate down to 1 kHz with a maximum L1 trigger rate of 100 kHz.

### 3.4 Event Cleaning

Beyond the reduction in the event storage rate handled by the trigger chains and prescaling, only select sections of the overall data output by the LHC are ever used in analyses. The LHC is not free from operational errors or issues with the hardware and software of the detector. Parts of the output data can be corrupted by incomplete events due to detector failings, poor data integrity or disruption of the machine. The operational time of the LHC

is split into Run sections, which are divided into luminosity blocks, time intervals of data recording where the experimental conditions are assumed to be constant. From the complete output for a Run section, only the blocks which have been marked as *good* are made use of in analyses. The internal directory of usable luminosity blocks is named the Good Runs List (GRL). Along with these event selections based on using correct data, analyses typically refine events down to a particular area of focus, which is discussed in Chapters 4, 5 and 6.

## 3.5 Object Reconstruction

### 3.5.1 Jets

As discussed in Section 2.2.3.3 the high  $p_T$  quarks and gluons produced during  $pp$ -collisions result in collimated streams of hadrons called jets, which are the physical objects detected in the event. Detectors make use of algorithms to reconstruct these jets from the calorimeter readouts to relate the stream of hadrons to the initial fragmented partons. There are various algorithms used to reconstruct jets within the ATLAS detector, and these algorithms commonly require the definition of a jet to be invariant under additional soft or collinear emissions. Such algorithms are designated as infra-red (IR) or collinear (C) safe.

Modern jet algorithms are broadly split into two types: cone-type and sequential clustering algorithms. Cone-type algorithms take the hardest (highest momentum) object in an event as a seed of an iterative process of looking for a stable cone rooted at this seed [62]. Once a cone is defined, any constituents contained within the cone are removed from consideration and the process repeats. The alternative sequential clustering algorithms assume that particles within jets will have small differences in transverse momentum and groups particles based on the momentum space to reconstruct the jets. Sequential clustering algorithms function using iterative steps with two distance parameters. The first distance is the separation between two particles  $d_{ij}$ , defined as

$$d_{ij} = \min(p_{Ti}^a, p_{Tj}^a) \frac{\Delta R_{ij}^2}{R}, \quad (3.2)$$

where  $a$  is a particular exponent for a given algorithm,  $R$  is the radius parameter of the final reconstructed jet size and  $\Delta R_{ij}$  is the  $(\eta, \phi)$  space distance between the two objects. The second parameter  $d_{iB}$ , is the momentum space distance between the beam axis and an object [63] and is given by

$$d_{iB} = p_{Ti}^a. \quad (3.3)$$

The principal algorithm used for jet reconstruction at ATLAS is the anti- $k_t$  algorithm [64], which is a sequential clustering algorithm with  $a = -2$ . The algorithm is seeded with the highest  $p_T$  topological clusters from the calorimeter cells in the event, and iteratively computes the distance parameters. At each step, the two are compared: if  $d_{ij}$  is smaller, particles  $i$  and  $j$  are combined whereas if  $d_{iB}$  is smaller particle  $j$  is labeled as a jet. The fact this algorithm tends to result in approximately circular reconstructed jet objects makes it favourable for experimental analyses as they are easily calibrated. The anti- $k_t$  algorithm is IRC safe and typical used with  $R = 0.4$  in the ATLAS experiment, and can be readily applied to clustering partons and calorimeter deposits in addition to hadrons.

During jet reconstruction, when the energy deposits are extracted from the calorimeter, there is the option of reading the calibrated [65] calorimeter cells according to the Electromagnetic (EM) scale, or by applying Local Cell (LC) corrections [66] to account for the attenuated physical response of the calorimeter and the difference in hadronic and electromagnetic response, which restores the energy of extracted objects to correspond to Monte-Carlo simulated truth objects. In this analysis, readouts of all jet objects, both offline and trigger level, were taken at the EM energy scale.

### 3.5.1.1 Pileup

As mentioned in Section 2.2.3.5 on the process of a  $pp$  collision, there are significant interactions as a result of the parton interactions accompanying the hard-scatter interaction of the collision. In addition to this underlying event, additional  $pp$ -collisions within a particular bunch crossing will contaminate the event. The collection of these jets from other  $pp$ -collisions in the detector output is termed in-time pileup [67]. In addition to the in-time pileup, interactions from preceding or subsequent bunch crossings also contribute contaminating objects to the detector readout, which is named out-of-time pileup. In-time and out-of-time pileup are collectively referred to as pileup in the detector, and necessitate processing and calibration of the detector output to remove the effects from consideration [68].

### 3.5.2 $b$ -Tagging

Hadrons containing a  $b$ -quark tend to feature a signature topology as a result of the long lifetime of  $b$ -hadrons. The extended lifetime results in a significant mean flight path of the  $b$ -hadron between its production and decay, typically around 3 mm transverse to the beam line, forming a displaced secondary vertex from the primary hard scatter interaction point. This distinctive structure can be used to identify  $b$ -jets, and algorithms that exploit this are known as lifetime-based tagging algorithms [69].

Identification of jets containing  $b$ -hadrons in ATLAS is based on combining the output of three separate lifetime-based  $b$ -tagging algorithms [70]: Impact Parameter based algorithms (IP2D and IP3D, Section 3.5.2.1), Secondary Vertex based (SV, Section 3.5.2.2) and Decay Chain based (JetFitter, Section 3.5.2.3) into a multivariate discriminant (MV2, Section 3.5.3) which is used to distinguish the jet flavours. These algorithms have undergone continuous improvement over the Run-2 cycle of the LHC to improve the separation of jet flavours.

The inputs for each of the  $b$ -tagging algorithms are taken from the ID of the ATLAS detector and the calorimeters (Sections 3.2.1 and 3.2.2). This limits  $b$ -tagging to jets with  $|\eta| < 2.5$ , and in addition jets with a  $p_T < 20$  GeV are not selected for  $b$ -tagging, nor jets determined to be likely a result of pileup in the detector which are eliminated using a multivariate discriminant from Jet Vertex Tagger algorithm [68, 71].

### 3.5.2.1 IP2D and IP3D: Impact Parameter based Algorithms

To identify  $b$ -hadron decays, impact parameters of tracks from the secondary vertex can be computed with respect to the primary vertex of the interaction. The IP2D algorithm uses a transverse impact parameter  $d_0$  defined as the distance of closest approach of a track to the primary vertex in  $(r, \phi)$  plane around the vertex. The IP3D algorithm uses both the transverse impact parameter and a correlated longitudinal impact parameter  $z_0$ , defined as the distance between the point of closest approach in  $(r, \phi)$  and the primary vertex in the longitudinal plane [72]. These parameters typically have large values as a result of the lifetime of  $b$ -quark. The signs of the impact parameters are also defined to take account of whether they lie in front or behind the primary vertex with respect to the jet direction, with secondary vertices occurring behind the primary vertex normally due to background.

The significance of the impact parameter values  $(\frac{d_0}{\sigma_{d_0}}, \frac{z_0}{\sigma_{z_0}})$  for each track are compared to probability density functions obtained from reference histograms derived from Monte Carlo simulation, with each track being compared to a selection of reference track categories. This results in weights which are combined using a log-likelihood ratio (LLR) discriminant to compute an overall jet weight separating between the three jet flavours:  $b$ -jets,  $c$ -jets from to  $c$  quarks, and light-jets from the  $u$ ,  $d$  and  $s$  quarks [69, 71].

### 3.5.2.2 SV1: Secondary Vertex Finding algorithm

The secondary vertex algorithm uses the decay products of the  $b$ -hadron to reconstruct a distinct secondary vertex [72]. The algorithm uses tracks that are significantly displaced from the primary vertex associated with the jet, forming vertex candidates for all pairs of track, while rejecting any vertices that would be associated with decay of long lived particles (e.g.  $\Lambda$ ), photon conversions or interactions with the material in the detector. The tracks forming these vertex candidates are then iteratively combined and refined to remove outliers beyond a  $\chi^2$  threshold leaving a single inclusive vertex.

The properties of this secondary vertex are used to differentiate the flavour of the jet. The SV1 algorithm is based on a LLR formalism similar to the IP algorithms, and makes use of the invariant mass of all charged tracks used to reconstruct the vertex, the number of two track vertices and the ratio of the invariant mass of the charged tracks to the invariant mass of all tracks. In addition the algorithm is signed in a similar fashion to the IP algorithms and uses the  $\Delta R$  between the jet direction and secondary vertex displacement direction in the LLR calculation. The algorithm uses distributions of these variables to distinguish between the jet flavours [69, 71].

### 3.5.2.3 JetFitter: Decay Chain Multi based Algorithm

The JetFitter algorithm exploits the topological structure of weak  $b$ -hadron and  $c$ -hadron decays inside the jet to reconstruct a full  $b$ -hadron decay chain. A Kalman filter is used to find a common line between the primary,  $b$ -hadron and  $c$ -hadron vertices to approximate the  $b$ -hadron flight path [73]. A selection of variables relating to the primary vertex and the properties of the tracks associated with reconstructed decay chain are used as input nodes in a neural network. This neural network uses the input variables,  $p_T$  and  $|\eta|$  variables from the jets, reweighted to ensure the spectra of the kinematics are not used in the training of the neural net. The neural network outputs discriminating variables relating to each jet flavour which are used to tag the jets [69].

### 3.5.3 Multivariate Algorithm

The output variables of the three basic algorithms described prior are combined as input into the Multivariate Algorithm MV2. MV2 is a Boosted Decision Tree (BDT) algorithm (Appendix B) which has been trained on  $t\bar{t}$  events to discriminate  $b$ -jets from light and  $c$ -jets. The kinematic properties of the training jets are included to exploit correlations with the other input variables, however the kinematic distributions of the signal  $b$ -jets and  $c$ -jets are reweighted to match the background light-jets to avoid the spectra being used as a

discriminating factor. The MV2 algorithm is a revised version of the MV1 algorithm used during Run-1 of the LHC, and has three sub-variants (MV2c00, MV2c10, and MV2c20) of the algorithm distinguished by the exact background composition of the training sample. The naming convention initially referred to the  $c$ -jet composition of the training sample; for MV2c20 the  $b$ -jets are designated as signal jets where a mixture of 80% light jets and 20%  $c$ -jets was designated as background [70].

The MV2 algorithm has a set of working points, defined by a single value of the output distribution of the algorithm, which are configured to provide a specific  $b$ -jet selection efficiency on the training  $t\bar{t}$  sample. Rather than being used independently, physics analyses will make use of several working points as an increase in  $b$ -jet efficiency (corresponding to *looser*  $b$ -jet selection) will bring an increased mistag rate of light and  $c$ -jets.

These algorithms were refined prior to the 2016 Run-2 data-taking session in response to  $c$ -jets limiting physics analyses more than the light-jets. This change to enhance the  $c$ -jet rejection meant that for the MV2c10, the  $c$ -jet fraction was set to 7% in training and the fraction for MV2c20 was 15%. There were a selection of other improvements made to the algorithm relating to the BDT training parameters and the use of the basic algorithms before the 2016 data taking. With these refinements, the MV2c10 algorithm was found to provide a comparable level of light-jet rejection to the original 2015 Mv2c20 algorithm with improved  $c$ -jet rejection, so was chosen as the standard  $b$ -tagging algorithm for 2016 analyses [71].

### 3.6 Trigger-Object Level Analysis

In physics analyses at the LHC, the 1kHz event readout rate to storage is significantly below the 40 MHz bunch crossing rate. This bottleneck is caused by the limited bandwidth (event rate  $\times$  event size in bytes) available to analysis channels. In searches with large backgrounds or those with low rates, the prescaling introduced in the trigger system critically affects the amount of significant events output to storage, limiting the statistical power of any search in these hard to isolate channels as a large number of events are discarded to keep output within bandwidth limitations.

This constraint can be alleviated by recording only a fraction of the detector readout for any given event, specifically the jet information reconstructed by the triggering system. This partial event corresponds to a reduction in the event size in bytes which allows for present bandwidth limitations to be upheld with an increased event rate. This process of using the objects produced in the trigger as substitutes for the offline objects is referred to as Trigger-Object Level Analysis (TLA) [12].

In these analyses, partially built events are collected using an additional TLA stream of the output data, which records the jet four-momentum along with a selection of additional identifying variables for jet objects in the HLT, triggered by jet objects from the L1 trigger. The readout does not include individual calorimeter cells nor information from the muon or tracking detectors, and in prior application of a TLA approach to a search for light dijet resonances [12] a partial TLA event was 5% of the size of a full detector readout, and TLA events were read out from the detector at a rate of 2 kHz.

## EVENT SELECTION

This chapter describes the selection criteria for data and simulated events, along with the specific calibrations and configurations used in the extraction and reconstruction of the objects making up the analysis. The event selections described here were chosen to target the typical VBF  $H \rightarrow b\bar{b}$  final state topology described in Section 2.3.4.

### 4.1 ATLAS Event Data

The raw data from the ATLAS detector is stored in a proprietary data format used by the ATLAS experiment, the Analysis Object Data (AOD) format. This is the output of the event reconstruction software, with each event having a corresponding discrete entry. For Run-2 of the LHC experiment, this was upgraded to the xAOD format, which is readable by ROOT [74], a modular software framework managed by CERN and designed specifically for analysis of large datasets with complex statistical analysis, visualisation of data and storage. The xAOD format is a many leveled branching tree structure, with nodes of the tree grouping together related information from each event, and has an associated Event Data Model (EDM) to standardise classes, interfaces and types for representation of an event facilitating simple analysis [75].

Analyses typically make use of a derivation framework to refine the complete xAOD into a more selective Derived xAOD (DxAOD) which will normally only contain the relevant objects to a target analysis, and results in a smaller dataset that is much easier to manipulate, store and operate over. These derivations are produced using the ATLAS bulk data pro-



cessing framework Athena [76]. The computation framework used for analysis of the xAOD data is the internally developed AnalysisBase suite of tools. The analysis presented in this dissertation uses AnalysisBase Release 2.4.31 and made use of the EventLoop package for event processing.

This set of tools is used for both the real event data and the simulated Monte-Carlo data, with DxAODs of both datasets forming the core data for any ATLAS physics analysis. These datasets, following from the large output rate of the LHC, are extremely large, necessitating the use of parallelised computation to perform any statistically significant analysis. The computational framework developed at ATLAS is designed to perform concurrent computation, and processing, making use of the Worldwide LHC Computing Grid [77] to provide the necessary hardware capacity.

## 4.2 Datasets

The proton-proton collision data was recorded at a centre-of-mass energy of  $\sqrt{s} = 13$  TeV in 2016. In this dissertation, Data Period D was used owing to limited storage space on analysis computing facilities. For events from the ATLAS detector to be considered usable for analysis, there are certain quality criteria that need to be passed by the event. Events are subdivided into luminosity *blocks*, which are marked as *good* if there are no flaws in the data integrity or missing information from the detector readout. The events were marked as *clean* if there were no errors reported for the tracker or calorimeter components of the detector, and only clean events were studied.

Information on whether certain luminosity blocks are marked as clean is contained within a configuration *Good Runs List* (GRL). This analysis used the all year 25 ns Good Runs List (Table A.1, Appendix A), resulting in a data luminosity of  $4.6 \text{ fb}^{-1}$ .

## 4.3 Monte-Carlo simulated events

The simulated VBF sample (Table A.1, Appendix A) was produced by Monte-Carlo event generators in 2015. This sample was produced using the NLO generator POWHEG [30] configured using the CTEQ6L1 [78] set of PDFs and interfaced with PYTHIA8 [28] tuned to AZNLO [79]. The response of the ATLAS detector to the Monte-Carlo events was simulated using the GEANT4 [80, 81] simulation, which recreates a configurable model of the ATLAS detector, and calibrations and reconstructions were executed identically using ATLAS reconstruction code on the Monte-Carlo simulated events and the real data.

To accurately compare the simulated events from the Monte-Carlo samples with the real event dataset, it is necessary to normalise the Monte-Carlo samples to the total luminosity of the dataset, based on the theoretical cross-section for the interaction. The Monte-Carlo simulation assigns a weight  $w_i$  to each event simulated, which are summed to give the total number of events in the Monte-Carlo sample. Each bin of any histogram in the results produced from the simulated data is reweighted using a scaling factor  $w_{MC}$ , given by

$$w_{MC} = \frac{\sigma k L}{N}, \quad (4.1)$$

where  $\sigma$  is the theoretical cross section,  $L$  the integrated luminosity of the real dataset,  $N$  the total number of simulated events ( $\sum_N w_i$ ) and  $k$  the Real  $K$ -Factor, which is a correction to the leading order cross section to reproduce the higher order calculation for the interaction. This reweighting of the Monte-Carlo datasets allows valid comparison of the Monte-Carlo simulated events with varying data sample sizes, as in the case of the reduced data luminosity in this analysis.

## 4.4 Jet Extraction

The analysis is based on the jet objects from the detector contained in the DxAOD, the reconstruction of which is covered in Section 3.5.1. Both the offline jet objects and the online equivalents are retrieved, but the method by which the full collection of jets is assembled differs in each case. For offline jet objects, the DxAOD contains a complete set of jets for each reconstruction algorithm, which are each associated with the relevant jet  $b$ -tagging information. Offline jets were calibrated in line with the 20.7 recommendations (Table A.2). In addition, recorded individual jets were required to have  $p_T > 45$  GeV.

Recovering the trigger-level jet objects from the xAOD is done by assembling distinct object collections from the data into a single jet collection. The jets that satisfied the trigger requirements (Section 4.5) are stored as *split*-jets in the data. These *split*-jet objects are those that will have  $b$ -tagging decisions associated with them. Any duplicate *split*-jets in this collection, determined by pairing jets and removing those with  $\Delta R$  spacings below a threshold value of 0.3 (Figure 5.1 in Chapter 5 shows the distribution of  $\Delta R$  values justifying this value), are removed and the  $b$ -tagging information stored in a separate xAOD container is associated with the *split*-jets. Following this all HLT trigger jets are retrieved. These HLT trigger jets are different from the *split*-jets and do not possess  $b$ -tagging information. The full set of HLT jets is compared to the *split*-jets and any duplicates are removed from the HLT jet collection (again using  $\Delta R$  matching) to form the *nonsplit*-jets. The combination of the *split*-jets and *nonsplit*-jets forms the complete jet collection for the trigger level event.

This complete collection of *split* and *nonsplit*-jets was taken as the comprehensive full set of jets for an event. The lack of associated *b*-tagging information for the *nonsplit*-jets meant only jets from the *split*-jet list could be designated as *b*-jets.

#### 4.4.1 *b*-jets

The details of *b*-jet identification are covered in Section 3.5.2. Offline *b*-jets were tagged using the MV2c10-tagger configured using the January 2017 recommendations (Table A.2) with two defined efficiency working points: *tight*, with an overall efficiency of 70% and *loose* with 85% tagging efficiency. Online *b*-jets were tagged using the MV2c20 -tagger as configured during the data taking, which made use of the March 2016 Recommendations (Table A.2) with two identically defined *tight* and *loose* working points. The use of the older *b*-tagging algorithm in the decision for the online jets was forced. The online trigger objects in the DxAOD only contain the results of the evaluated *b*-tagging, the quantities used during the calculation were previously discarded. As such, this analysis was required to use the MV2c20 algorithm for HLT jets.

### 4.5 VBF $H \rightarrow b\bar{b}$ Analysis Strategy

Candidate VBF  $H \rightarrow b\bar{b}$  events are selected by requiring two *central* *b*-jets which form the Higgs boson candidate and two high  $p_T$  VBF-tagging jets. The analysis presented in this dissertation follows the selection criteria outlined in the 2016 Search for VBF  $H \rightarrow b\bar{b}$  at ATLAS [11]. Searches using VBF  $H \rightarrow b\bar{b}$  consider two exclusive analysis channels of interesting events: the *four-central* channel, which requires all four jets to be contained within the central region  $|\eta| < 2.8$ , and the *two-central* channel which requires two jets in the central region and at least one forward jet. The analysis presented in this dissertation focuses on the *two-central* channel as this is a more standard VBF topology.

For the *two-central* channel, the event was required to pass the HLT\_j80\_bmv2c2070\_split\_j60\_bmv2c2085\_split\_j45\_320eta490 trigger. This trigger requires a single L1 jet RoI of  $E_T > 40$  GeV and  $|\eta| < 2.5$ , a second central jet RoI with  $E_T > 25$  GeV, and a forward jet RoI with  $E_T > 20$  GeV and  $3.1 < |\eta| < 4.9$ . At the HLT, one central jet *b*-tagged at the *tight* working point with  $p_T > 80$  GeV, and a jet with  $p_T > 60$  GeV tagged at the *loose* working point were both required. Finally a HLT forward jet with  $p_T > 45$  GeV between  $3.2 < |\eta| < 4.9$  was needed.

Once the trigger was passed, the event was required to contain one jet with  $p_T > 95$  GeV which was *b*-tagged at the *tight* working point and one additional jet with  $p_T > 70$  GeV that passed the *loose* *b*-tagging working point. One forward jet with  $3.2 < |\eta| < 4.4$  and

$p_T > 60$  GeV was required along with a final VBF jet with  $p_T > 20$  GeV and  $|\eta| < 4.4$ . Finally the  $p_T$  of the  $b\bar{b}$  pair was required to exceed 160 GeV. This cut is to remove kinematic sculpting of the  $M_{bb}$  distribution, which for absent or lower  $p_{Tbb}$  cuts has a pronounced bump in the 200-300 GeV  $M_{bb}$  region. This bump is a result of the correlation between  $m_{bb}$  and  $p_{Tbb}$  values. By requiring the  $p_{Tbb}$  cut, the  $m_{bb}$  distribution forms a regular falling distribution. The cuts as applied in the analysis code are summarised in Table 4.1

**Table 4.1:** Cutflow for the *two-central* VBF  $H \rightarrow b\bar{b}$  channel.

Cut	Description
Good Runs List	Event required to pass GRL.
Clean Events	Event required to be unaffected by detector issues.
Trigger	Event required to have passed the HLT_j80_bmv2c2070_split_j60_bmv2c2085_split_j45_320eta490 trigger.
$\geq 2$ loose	Event was required to contain at least two $b$ -jets with $p_T > 70$ GeV tagged at the <i>loose</i> working point.
$\geq 2$ light-jets	Event was required to contain at least two non- $b$ -jets with $p_T > 20$ GeV.
<i>Tight</i> $b$ -jet	Event was required to contain one $b$ -jet with $p_T > 95$ GeV tagged at the <i>tight</i> working point.
Forward jet requirement	Event was required to contain one non- $b$ -jet with $p_T > 60$ GeV and $3.2 <  \eta  < 4.4$ .
$p_{Tbb} > 160$ GeV	The chosen $b\bar{b}$ pair was required to have a combined $p_T > 160$ GeV

The events were required to be clean events, unaffected by any small detector issues, and the jets were assigned to components of the VBF  $H \rightarrow b\bar{b}$  event as described in the following procedure. All pairs of jets that passed the *loose* working point (where either of the jet pair passed the *tight* working point) were considered; the pair with the highest  $p_{Tbb}$  was selected as the Higgs candidate. An identical iterative procedure was carried out to assign the VBF pair, using jets not marked for consideration as the Higgs boson candidate. One of the VBF jet pair was required to satisfy the forward jet selection criterion, and the highest invariant mass pair was selected.

These conditions were identical for both the Monte-Carlo simulation and data, with the exception of the trigger requirements which were not required for the simulated samples.

In a full ATLAS analysis [11], the signal is extracted from the selected events using a Boosted Decision Tree (BDT) trained to extract the VBF  $H \rightarrow b\bar{b}$  events over non-Higgs backgrounds. Time constraints in this analysis prohibited a full BDT analysis, but discussion of boosted decision trees and training is covered in Appendix B.

## OBJECT PERFORMANCE

Prior to conducting a full study of TLA on the VBF  $H \rightarrow b\bar{b}$  channel, the features of jet objects reconstructed offline and within the HLT were compared to identify any performance differences in the base components of event reconstruction. The jet objects were compared on a one-to-one basis, with online jets matched to offline jets by requiring the  $\Delta R$  (Section 2.2.2) value between the two jets to be below a threshold value of 0.3. This cut was determined from a plot of  $\Delta R$  values between all pairs of jets, shown in Figure 5.1.

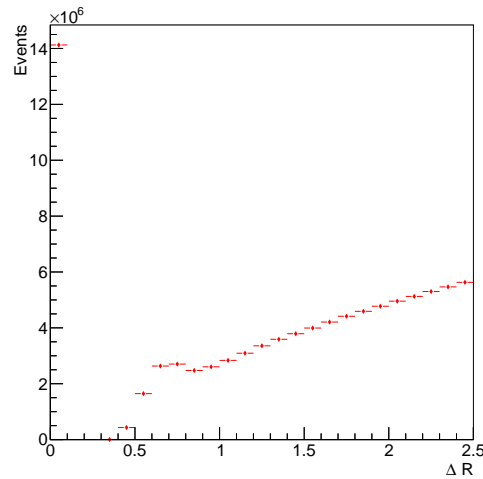


**Figure 5.1:** Plot of  $\Delta R$  values for all online/offline jet pairs taken from the Monte-Carlo simulations. The large spike at  $\sim 0$  accounts for matching jets, with the higher  $\Delta R$  values corresponding to differing jet pairs.

To compare the online and offline jets, the fractional difference in value for a variety of jet kinematic properties between the matched jets were evaluated. These values were calculated for jet feature  $X$  using the ratio of the difference between the offline and online jet features to the offline jet feature

$$\frac{\Delta X}{X} = \frac{X_{Offline} - X_{Online}}{X_{Offline}}, \quad (5.1)$$

where  $X_{Offline}$  is the value of the kinematic quantity for the offline jet and  $X_{Online}$  is the same quantity for the HLT jet. Of the kinematic jet quantities, jet  $p_T$  was the most significant value to study for a VBF  $H \rightarrow b\bar{b}$  analysis. In addition, the jet  $\eta$  and  $\phi$  values were compared to assess similarities between the topological distributions of the HLT and offline jets.

These key kinematic quantities were studied for both the leading  $b$ -jet and the leading non- $b$ -jet of an event given these jet types make up a VBF  $H \rightarrow b\bar{b}$  event. The jet objects were also divided into buckets of pseudo-rapidity described in Table 5.1 to examine any changes in behaviour in  $\eta$ , as any differences will significantly impact any assessment of the forward VBF  $H \rightarrow b\bar{b}$  jets.

**Table 5.1:** Pseudorapidity bands.

Jet Designation	$\eta$ Range
Central	$0 <  \eta  < 1$
	$1 <  \eta  < 2.4$
Forward	$2.4 <  \eta  < 4.9$

The jets used to produce these plots were taken from all analysed Monte-Carlo events and all data events where the HLT\_j80\_bmv2c2070\_split\_j60\_bmv2c2085\_split\_j45\_320eta490 trigger was passed, but the additional VBF  $H \rightarrow b\bar{b}$  requirements mentioned in Section 4.5 were not enforced. In addition, given the  $p_T$  requirements of the desired event are high, only jets with  $p_T > 45$  GeV were considered for analysis.

## 5.1 Leading $b$ -jets

The leading  $p_T$  offline  $b$ -jet was selected from an event, requiring the jet to pass the tight  $b$ -tagging working point. This jet was matched to a corresponding online jet using  $\Delta R$  matching, and the properties of each of these jets compared in both data and Monte-Carlo simulations. The  $\frac{\Delta p_T}{p_T}$  distribution for both the Monte-Carlo and data with respect to the  $p_T$  of the leading  $b$ -jet is shown in Figure 5.2.

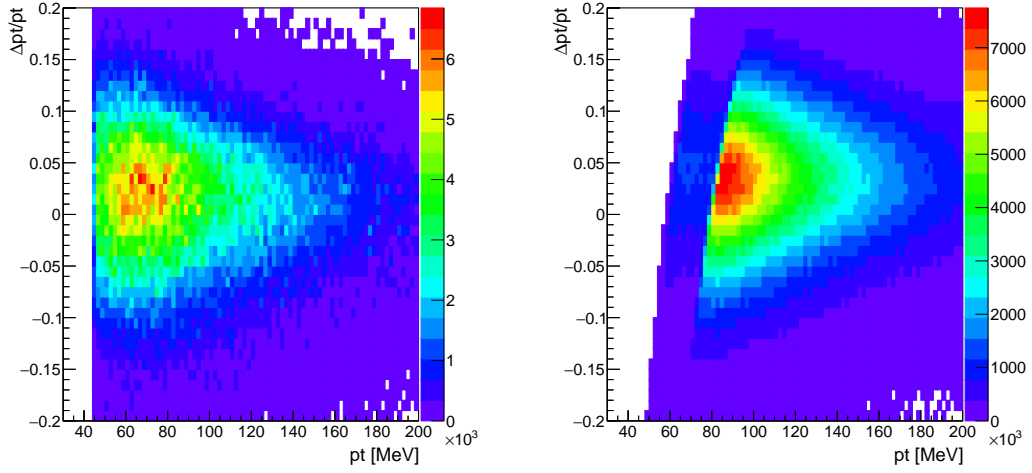


**Figure 5.2:**  $\frac{\Delta p_T}{p_T}$  for the leading  $p_T$   $b$ -jet against  $p_T$  of the offline  $b$ -jet, plotted for Monte-Carlo simulation in the left panel and data in the right panel.

The comparative performance of the online and offline jets in  $p_T$  is broadly similar for events in both data and Monte-Carlo simulations. The bulk of the results occur with a  $0 < \frac{\Delta p_T}{p_T} < 0.05$  and the two plots show a comparable distribution drop off, both showing a maximum  $\frac{\Delta p_T}{p_T}$  width of  $-0.1 < \frac{\Delta p_T}{p_T} < 0.15$  and showing the  $p_T$  distribution reaching a maximum of  $\sim 80$  GeV. The distinctive curved edge starting at  $p_T \sim 80$  GeV present in the real data is the result of the trigger being applied to each event, which was not applied in the Monte-Carlo simulation. The trigger requires at least one jet with a  $p_T > 80$  GeV which results in the small number of events below this cut value.

The curve of the distribution shown in the right panel of Figure 5.2 can be explained given  $\frac{\Delta p_T}{p_T}$  is predominantly positive. In the average case based on this, the  $p_T$  of the offline jet is higher than the online jet. As the trigger is evaluated on the online jet, only events with an online  $p_T > 80$  GeV will be entered into this histogram. For an offline jet with  $p_T = 85$  GeV to have  $\frac{\Delta p_T}{p_T} = 0.1$ , the online jet would be less than the trigger  $p_T$  cut and as such will not enter into the plot shown in Figure 5.2. This exclusion of certain  $\frac{\Delta p_T}{p_T}$  values for certain offline  $p_T$  values follows from the demonstrated bias in  $\frac{\Delta p_T}{p_T}$ , and produces the curved edge of the distribution.

The distribution of the  $\frac{\Delta p_T}{p_T}$  about zero can be shown in more detail by taking a slice across the distribution for a representative  $p_T$  value, which is shown in Figure 5.3 for leading  $b$ -jets with  $89 < p_T < 91$  GeV. The  $\frac{\Delta p_T}{p_T}$  values were also split into the  $\eta$  bands from Table 5.1. For the leading  $b$ -jet, this is constrained to be within the region of the detector where  $b$ -tagging is available, so the forward band is excluded.

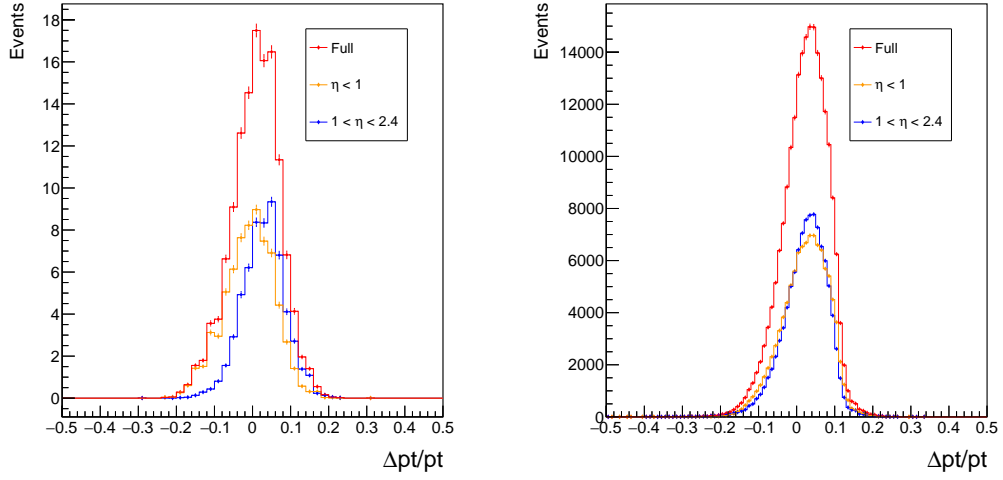


**Figure 5.3:**  $\frac{\Delta p_T}{p_T}$  distribution for the leading  $b$ -jet with  $89 < p_T < 91$  GeV. The distributions for all events and events split by  $\eta$  region are shown. Monte-Carlo simulation is shown in the left panel and data in the right panel.

The results show similar profiles between the Monte-Carlo and Data events for  $\frac{\Delta p_T}{p_T}$ . Both plots show the median offline  $p_T$  values to be higher than the online, with a median shift of 4% in data and 2% in Monte-Carlo simulations. The performance between  $\eta$  ranges was also consistent. The profiles broadly match the full shape of each other, but the Monte-Carlo plot in the left panel of Figure 5.3 showed a slight difference in  $\frac{\Delta p_T}{p_T}$  value as the central  $\eta$  range peaked at approximately zero. The breadth of these distributions is quite large, with the data and Monte-Carlo simulations showing a  $\frac{\Delta p_T}{p_T}$  distribution width of  $\sim 20\%$  about 0.

This offset of the median  $\frac{\Delta p_T}{p_T}$  value shows that there is a difference in the jet energy calibration between the HLT and the offline reconstruction. The difference between the two is also shown by the offset peaks of the  $\eta$  bands in Figure 5.3, with the more central region performing better. Prior calibration studies of the ATLAS calorimeter have shown the energy readouts to be more consistent towards the central regions of the detector [82]. This could cause the inaccuracy of the trigger jets in the higher pseudorapidity regions, as offline jet reconstruction can make use of developed calibration tools to account for these differences. Using these standard tools, the energy scale calibration difference between the offline and online jets can be rectified for future analyses [82, 83].

The  $\frac{\Delta X}{X}$  comparisons can be carried out for the topological jet properties ( $\eta$ ,  $\phi$ ) to confirm the offline and online jets are positioned within the detector in a similar fashion. Plots of  $\frac{\Delta \eta}{\eta}$  against the pseudorapidity of the offline jet in the selected pair for data and Monte-Carlo simulation are shown in Figure 5.4, and comparable plots of  $\frac{\Delta \phi}{\phi}$  against the offline  $\phi$  are given in Figure 5.5.



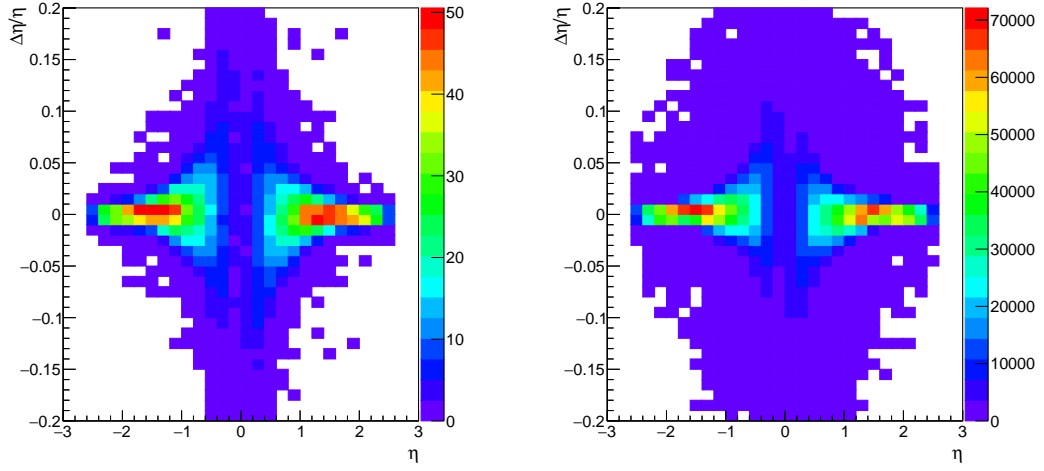


**Figure 5.4:**  $\frac{\Delta\eta}{\eta}$  for the leading  $b$ -jet, for Monte-Carlo simulation in the left panel and data in the right panel.

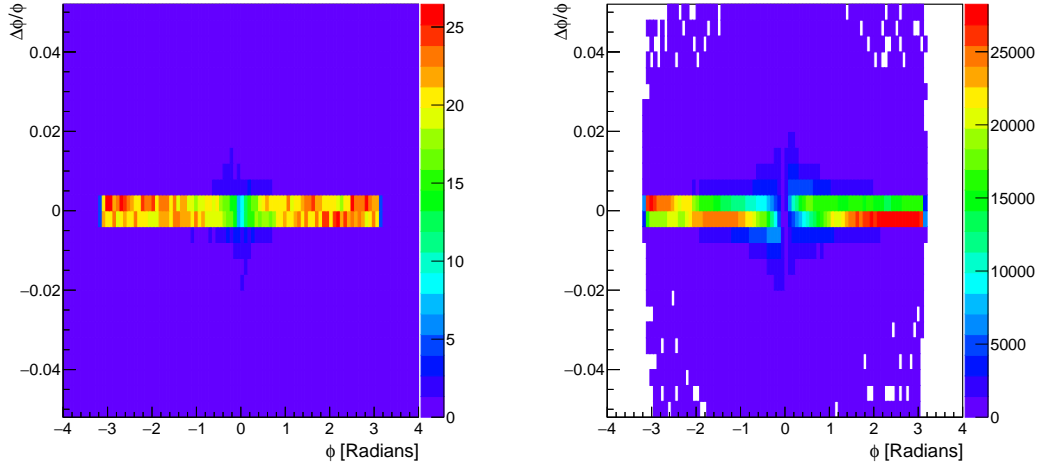


**Figure 5.5:**  $\frac{\Delta\phi}{\phi}$  for the leading  $b$ -jet, for Monte-Carlo simulation in the left panel and data in the right panel.

The data and Monte-Carlo distributions for these values are extremely similar to each other, and also show very close agreement between the values for offline and online jet objects. For both  $\frac{\Delta\eta}{\eta}$  and  $\frac{\Delta\phi}{\phi}$  the median value is approximately zero and the width of the distribution is less than 1% of the value. These results show the  $(\eta, \phi)$  positions of the online and offline jet objects are comparable to each other.

## 5.2 Leading Non $b$ -jets

For VBF  $H \rightarrow b\bar{b}$ , a pair of high  $p_T$  forward jets is the other significant feature, so the offline/online performance in the leading non- $b$ -jet was studied. Identically to the analysis of the leading  $b$ -jet in Section 5.1, the  $p_T$ ,  $\eta$  and  $\phi$  values of a matched offline/online jet pair were studied by calculating  $\frac{\Delta X}{X}$  values and plotting against the offline kinematic quantity. The results could be split into the  $\eta$  bands from Table 5.1, with the forward pseudorapidity band available for analysis as  $b$ -tagging was not required. Plots of  $\frac{\Delta p_T}{p_T}$  for the leading non- $b$ -jet are shown in Figure 5.6.

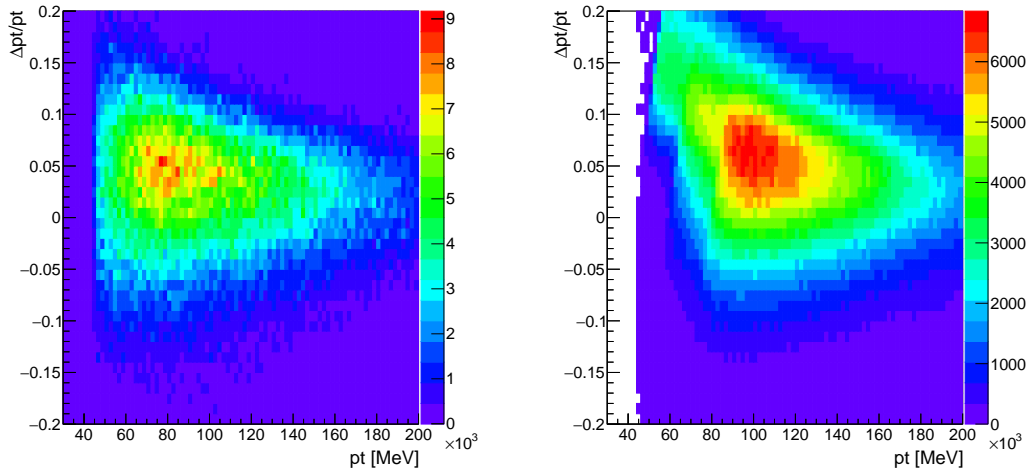


**Figure 5.6:**  $\frac{\Delta p_T}{p_T}$  for the leading  $p_T$  non- $b$ -jet against  $p_T$  of the offline jet, plotted for Monte-Carlo simulation in the left panel and real data in the right.

The leading non- $b$ -jet distributions show similar results to the leading  $b$ -jet distributions in Figure 5.2. The peak of the distribution between  $0 < \frac{\Delta p_T}{p_T} < 0.1$  shows there is agreement between the  $p_T$  of the offline and the online non- $b$ -jet. The overall shape of the distribution shows some differences between the Monte-Carlo simulation and data. The distributions are similarly structured, with a  $\frac{\Delta p_T}{p_T}$  width between  $-0.1$  and  $0.15$  and the  $p_T$  offline distribution reaching a maximum value of  $\sim 180$  GeV. However, there is a distinct cluster of results shown only in the right panel of Figure 5.6 of low  $p_T$  offline jets with  $\frac{\Delta p_T}{p_T} > 0.1$ . This bulge is likely caused by the different calibrations applied to trigger and offline jets. The default jet energy scale calibration is known to need large in-situ corrections in different regions of the calorimeter and these are applied only to the offline jets as shown in Table A.2, so differing responses are expected. In addition, Figure 5.7 shows the origin of the bulge could be due to jets reconstructed in the forward calorimeter, which are peaked toward higher  $\frac{\Delta p_T}{p_T}$  values than jets from other calorimeter. There is also a suggestion of a curving edge to the

distribution for the data, in an opposite direction to that shown for the leading  $b$ -jet in Figure 5.2. In addition, the peak of the data is slightly higher in  $p_T$  ( $\sim 80$ -120 GeV) than in the Monte-Carlo simulations ( $\sim 60$ -110 GeV).

The slight upward shift in  $p_T$  can be explained by the  $p_T$  requirements of the trigger applied only to the data. Requiring the jet components to exceed high  $p_T$  cuts will bias the results to events containing high  $p_T$  jets, accounting for the upward  $p_T$  shift of the data events in the right panel of Figure 5.6 relative to the left.

As for the leading  $b$ -jet, slices can be taken of the  $\frac{\Delta p_T}{p_T}$  distribution to show the spread of values more clearly. Plots of  $\frac{\Delta p_T}{p_T}$  values for leading non- $b$ -jets with  $89 < p_T < 91$  GeV are shown for Monte-Carlo simulation and data in Figure 5.7, and results have been split into the pseudorapidity bands from Table 5.1.

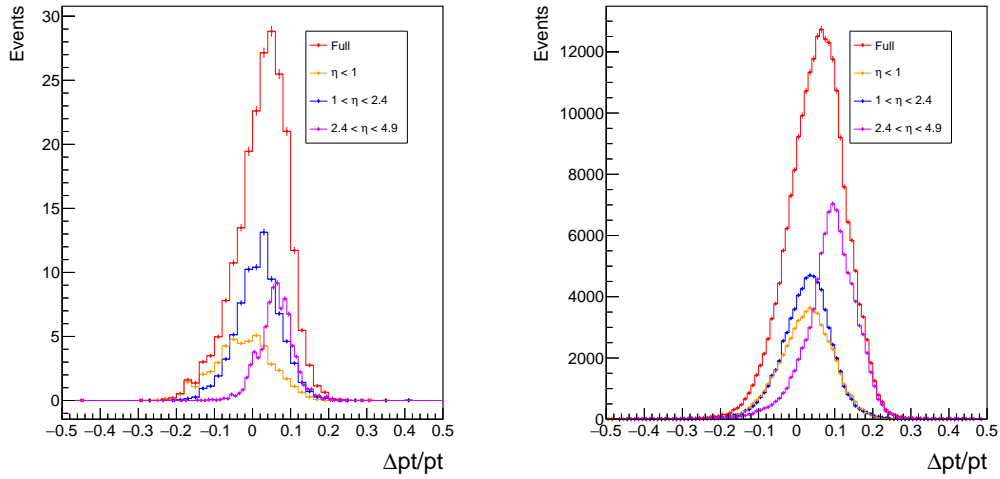


**Figure 5.7:**  $\frac{\Delta p_T}{p_T}$  distribution for the leading non- $b$ -jet, with  $89 < p_T < 91$  GeV plotted for Monte-Carlo simulation in the left panel and data in the right panel. The distributions for all events and events split by  $\eta$  region are shown.

Both Monte-Carlo simulations and data show the median value for offline jet  $p_T$  to be higher than the online jet by 4% and 6% respectively. The overall distribution shape is similar between the simulated and real events for the full set of results, but the distributions for the  $\eta$  bands differ between the Monte-Carlo simulations and the data.

The Monte-Carlo results for the central  $\eta$  band show a dip in  $p_T$  at the centre of the distribution and are shifted in  $\frac{\Delta p_T}{p_T}$  towards the negative. Both the data and Monte-Carlo show that the  $\frac{\Delta p_T}{p_T}$  value is much closer to zero for the two central  $\eta$  bands than the forward band, which peaks significantly higher than the median  $\frac{\Delta p_T}{p_T}$  value. The offset of the forward  $\eta$  band from the median is much worse for the data in the right panel of Figure 5.7. In addition, the relative proportions of the three  $\eta$  bands differ. In Monte-Carlo results most

jets fell in the middle  $1 < |\eta| < 2.4$  region, while the data showed significantly more forward jets.

The relatively increased proportion of forward jets is likely a consequence of the HLT\_j80\_bmv2c2070\_split\_j60\_bmv2c2085\_split\_j45\_320eta490 trigger being applied to the data. As the data events are required to have a forward jet to be stored in the histogram, this will bias the results to contain a greater proportion of forward jets, leading to the larger peak.

The  $\frac{\Delta p_T}{p_T}$  results for the leading non- $b$ -jet as for the leading  $b$ -jet show a difference in energy calibration between the HLT jet objects and the reconstructed offline objects. This difference in calibration can be corrected using standard jet calibration tools to bring the  $p_T$  values into closer agreement with one another [82, 83].

These  $\frac{\Delta X}{X}$  values can be calculated and plotted for the topological kinematic quantities  $(\eta, \phi)$ , with  $\frac{\Delta \eta}{\eta}$  for the leading non- $b$ -jet plotted in Figure 5.8 against the offline jet  $\eta$ , and  $\frac{\Delta \phi}{\phi}$  against offline  $\phi$  plotted in Figure 5.9. As with the  $b$ -jets the  $(\eta, \phi)$  values of the offline and online jets produce nearly identical results, with the distribution of  $\frac{\Delta X}{X}$  firmly centred around 0 and a width of less than 1%. As with the  $b$ -jets, this shows the spatial position of the leading non- $b$ -jet is comparable for online and offline objects.

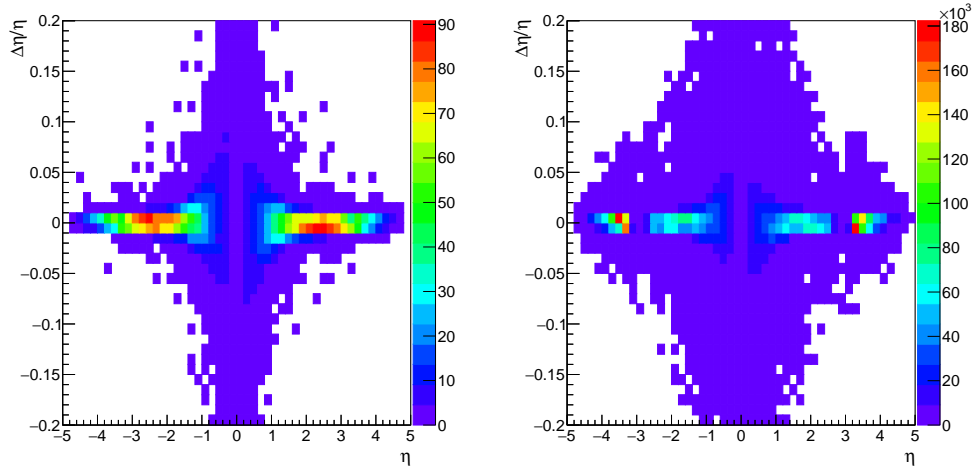


**Figure 5.8:**  $\frac{\Delta \eta}{\eta}$  for the leading non- $b$ -jet, for Monte-Carlo simulation in the left panel and data in the right panel.

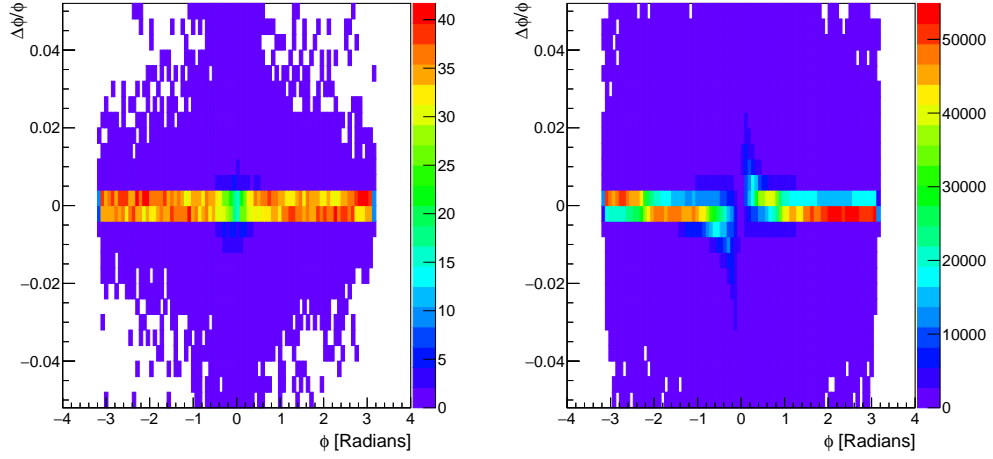


**Figure 5.9:**  $\frac{\Delta\phi}{\phi}$  for the leading non- $b$ -jet, for Monte-Carlo simulation in the left panel and data in the right panel.

### 5.2.1 Summary of Comparison of Jet Objects between Offline and Online

The jet objects reconstructed in the HLT have some slight differences in the reported values for key topological variables, but overall they perform in a similar fashion, both in Monte-Carlo simulations and in data. The positional variables  $\phi$  and  $\eta$  are directly comparable between offline and online jet objects, with the majority of objects having values with  $< 1\%$  disagreement for both  $b$ -jets and non- $b$ -jets. For the  $p_T$  of jet objects, the values are not in perfect agreement, but have a consistent offset observed in Monte-Carlo simulation and data.

This difference in jet energy scale calibration can easily be overcome by constructing or using specific online jet calibrations using already standard jet calibration tools [82, 83] to correct the offset of the  $p_T$  values.

With this calibration executed on the HLT jet objects, the online jets would then be directly comparable in energy scale and topographical location to the offline jet objects, and as such would be usable in analyses as a replacement for the offline objects. Further verification of this could be carried out by emulating the trigger for the Monte-Carlo simulation to check if the same features arise in the kinematic quantity distributions.

### 5.3 Jet Tagging Efficiency

As covered in Section 3.5.3, the standard algorithm for 2016 physics analyses was chosen to be the 2016 MV2c10 algorithm. However, the HLT  $b$ -tagging algorithm uses the older MV2c20 algorithm [59]. For any form of a Trigger Level Analysis to be considered valid, the performance of the tagging algorithms used in the trigger, which are fixed at the point of data collection, must be comparable with the tagging executed offline with more up to date  $b$ -tagging configurations.

To study this, the  $b$ -tagging efficiency at trigger level and offline is studied for different jet flavours using the Monte-Carlo sample. The Monte-Carlo sample was used as the *truth* nature of the jet object is known, and the result of the  $b$ -tagging algorithm can be compared for  $b$ -jets,  $c$ -jets and light-jets.

In the analysis, an offline/HLT jet pair was formed using  $\Delta R$  matching and using the truth label of the offline jet to assign a flavour to the pair. Light-jets,  $b$ -jets and  $c$ -jets were all studied separately to view the  $b$ -tagging efficiency and the mistag rate of both algorithms operating at the tight working point for an expected  $b$ -tagging efficiency of 70%. The efficiency plots in Figures 5.10, 5.11 and 5.12 show the fraction of these jets that were identified as  $b$ -jets by the HLT and offline tagging algorithms. These plots were created from events following the same cuts as for the leading  $b$ -jet and non- $b$ -jet as discussed at the beginning of the chapter.

#### 5.3.1 $b$ -jet efficiency

For jets labeled as true  $b$ -jets, the tagging efficiency can be calculated and plotted against kinematic quantities of the  $b$ -jets. Figure 5.10 shows the  $b$ -tagging efficiency  $\epsilon$  plotted against the  $p_T$  and  $\eta$  of the offline  $b$ -jet.

The overall distribution shape in  $p_T$  and  $\eta$  for the  $b$ -tagging efficiency is consistent for both the online and offline  $b$ -jet. The shape of the distribution in  $p_T$  shown in the left panel of Figure 5.10 is consistent with the efficiency curves expected for the MV2  $b$ -tagging algorithm with respect to  $p_T$  [71], and the efficiency is consistent with the 70% value expected for the tight working point for the offline jets, shown clearly by the flat peak of the  $\eta$  distribution in the right panel for the central  $\eta$  regions.

However, the HLT  $b$ -tagging is shown to be around 5% less efficient than the offline  $b$ -tagging for jets with  $p_T > 50$  GeV. This value is consistent across the  $p_T$  distribution shown by the flat line at  $\sim 0.95$  in the ratio plot in the left panel of Figure 5.10. The improvement in efficiency between the 2016 MV2c10 and 2015 MV2c20 algorithms is consistent with the comparative behaviour shown for a training  $t\bar{t}$  sample [71], but of a

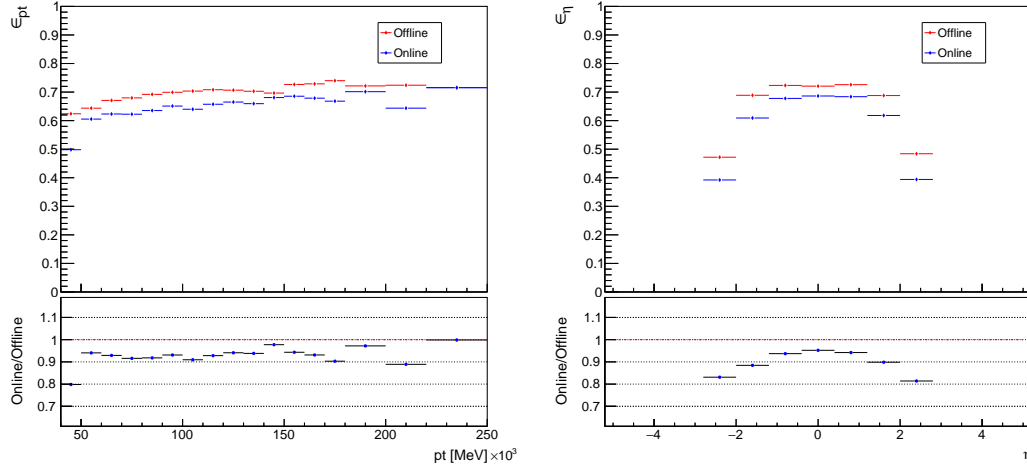


**Figure 5.10:**  $b$ -tagging efficiency for truth  $b$ -jets in Monte-Carlo simulation, evaluated for offline jets with the 2016 MV2c10 algorithm and for online jets with the 2015 MV2c20 algorithm, plotted against offline jet  $p_T$  in the left panel and offline jet  $\eta$  in the right panel.

larger magnitude. The performance will also differ as the computational time available for the online algorithm is greatly reduced compared to the offline tagging. This requires a less precise tracking algorithm which will perform slightly worse than the offline algorithm, which should account for some of the difference.

This change in efficiency, consistent with the differences in the two algorithms, could be rectified by applying the newer algorithm to the online jet objects. However, the trigger-level jet objects in the xAOD sample data only contained the discriminant values from the applied 2015 MV2c20 algorithm which could be extracted using standard  $b$ -tagging tools in AnalysisBase. The input variables used for the training and evaluation of the component algorithms of the MV2 algorithms (Section 3.5.2) were discarded from the HLT level jet objects. Retaining these quantities on the online jets would allow future trigger-level analyses to make use of the newer  $b$ -tagging algorithms or retrain one algorithm to increase the performance to offline levels. This would result in an increased detector readout size in bytes, which could reduce the possible rate increase from a TLA. An estimate of such a resultant decrease in rate requires further work beyond the scope of this dissertation.

### 5.3.2 $c$ -jet efficiency

The same efficiency plot could be produced for  $c$ -jets against the kinematic jet quantities. Any result marked as a  $b$ -jet for a truth  $c$ -jet is a mistagged jet, and plots of the efficiency show measurements of the mistag rate of the algorithm. The mistag rate is plotted in Figure 5.11 for the online and offline jets against offline  $p_T$  and  $\eta$ .

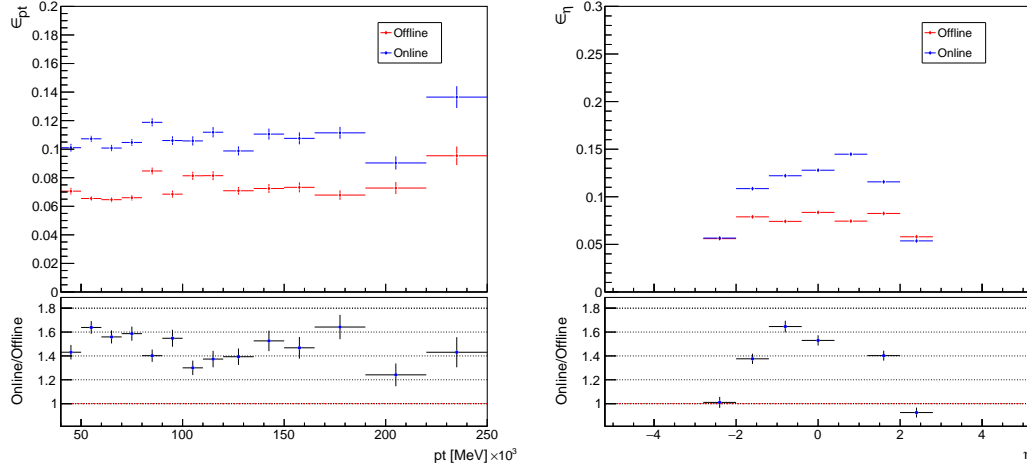


**Figure 5.11:** Mistag rate for truth  $c$ -jets in Monte-Carlo simulation, evaluated for offline jets with the 2016 MV2c10 algorithm and for online jets with the 2015 MV2c20 algorithm, plotted against offline jet  $p_T$  in the left panel and offline jet  $\eta$  in the right panel.

The shape of the mistag rate distribution is more noisy than the  $b$ -jet efficiency plots in Figure 5.10, but across the  $p_T$  distribution in the left panel of Figure 5.11 the online mistag rate is  $\sim 50\%$  higher than the offline rate.

The increase in the rate of  $c$ -jet mistagging is absolutely consistent with the refinements to the algorithm between the 2016 MV2c10 and 2015 MV2c20, with increased levels of  $c$ -jet rejection in the offline 2016 MV2c10, and the increase is consistent with the expected shift from the optimised algorithm [71]. Similar to the solution for changes in  $b$ -tagging efficiency in Section 5.3.1, retaining the inputs to the  $b$ -tagging algorithms would allow improved versions of the algorithms to be applied to the HLT jets.

### 5.3.3 Light-jet efficiency

Plots of the mistag rate for truth light-jets for online and offline  $b$ -tagging against the offline jet  $p_T$  and  $\eta$  are shown in Figure 5.12

The light-jet efficiency plots are noisier than the plots for truth  $b$ -jets and  $c$ -jets owing to the low mistag rate of  $\sim 0.3\%$ , as shown in the left panel of Figure 5.12. For these light-jets, the online algorithm performs better than the offline algorithm overall, with a mistag rate of equal to  $\sim 80\%$  the offline rate for jets with  $p_T < 150$  GeV. The change in the performance for the light-jet rejection, with the 2015 MV2c20 algorithm performing better for higher  $p_T$  values and worse for lower  $p_T$  values, is consistent with the expected change in behaviour between the two algorithms [71].



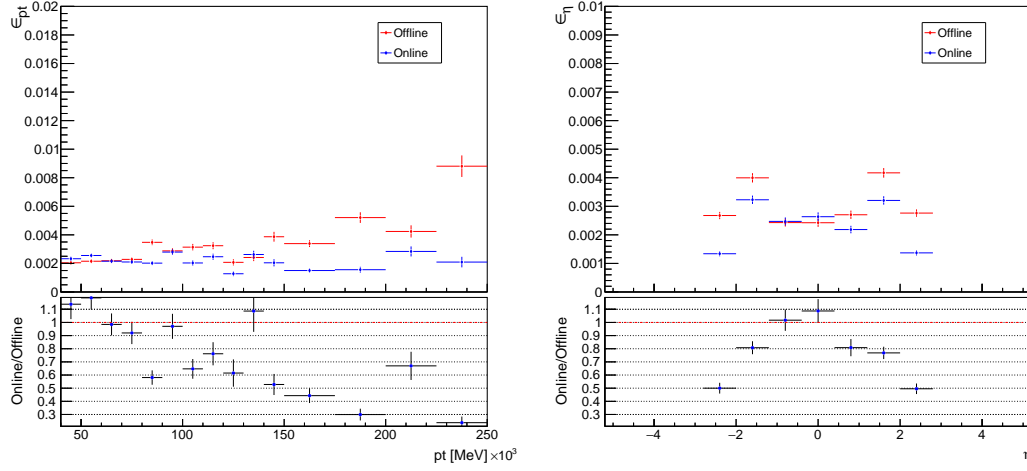


**Figure 5.12:** Mistag rate for truth light-jets in Monte-Carlo simulation, evaluated for offline jets with the 2016 MV2c10 algorithm and for online jets with the 2015 MV2c20 algorithm, plotted against offline jet  $p_T$  in the left panel and offline jet  $\eta$  in the right panel

## 5.4 Summary

The aim of this section of the analysis was to show that using online reconstructions of the constituent jet objects used in a VBF  $H \rightarrow b\bar{b}$  analysis was comparable to using offline objects by showing the properties of the jets and the  $b$ -tagging of the jets to be similar. The overall performance using the HLT objects as constructed during the data-taking and in the Monte-Carlo simulations is similar to the offline behaviour. The topological jet quantities ( $\eta$ ,  $\phi$ ) are directly comparable between the two types of jet objects. However there are differences between the  $p_T$  values of the HLT and offline jet objects and differences between the performances of the  $b$ -tagging algorithms.

These differences are readily rectifiable however. The energy scale calibration differences can be accounted for using standard jet calibration tools to bring the  $p_T$  values of the online and offline jets into agreement with one another [82], while the  $b$ -tagging performance can be made similar if the input variables to the MV2 algorithm are preserved on the trigger-level jet object, such that more developed  $b$ -tagging algorithms can be applied to the jet instead of the algorithm used during data collection.

With these corrections, there are no differences between the trigger level objects making up a VBF  $H \rightarrow b\bar{b}$  event and the offline objects that would prohibit a TLA analysis of the VBF  $H \rightarrow b\bar{b}$  channel.

## VBF $H \rightarrow b\bar{b}$ ANALYSIS

After finding the base constituents of the VBF  $H \rightarrow b\bar{b}$  event at the offline and HLT levels to be similar in behaviour, the specific objects that make up a VBF  $H \rightarrow b\bar{b}$  event can be studied and compared. In this chapter, the events were required to pass all cuts discussed in Section 4.5.

### 6.1 Cutflow

Prior to investigating the kinematic variables of the VBF  $H \rightarrow b\bar{b}$  event and the variables used for the BDT training (Appendix B), the event cutflow for both the Monte-Carlo simulations and data should be studied to highlight any differences between the event counts. These counts are given in Table 6.1, and the ratio of the events is shown in Figures 6.1 and 6.2.

#### 6.1.1 Monte-Carlo

The online performance has fewer events than the offline for all points in the cutflow, and overall produces  $\sim 82\%$  of the total signal events. There are three distinct jumps in the cutflow ratio: at the cuts on the *loose*  $b$ -jets, light-jets and the forward jet requirement, of  $\sim 7\%$  each. As shown in Figure 5.10, online  $b$ -tagging is  $\sim 93\%$  as efficient as the offline  $b$ -tagging in Monte-Carlo simulations. When considering tagging two distinct  $b$ -jets, any difference in efficiency is squared. Given the difference in tagging rates, this would result in  $\sim 86\%$  tagging efficiency for two  $b$ -jets, which is lower than shown in the cutflow. As

**Table 6.1:** Cutflow for the *two-central* VBF  $H \rightarrow b\bar{b}$  events as described in Section 4.5. The cutflows are given for the online and offline channels in both data and Monte-Carlo.

Cut	MC Offline	MC Online	Data Offline	Data Online
Clean Events	6229.48	6229.48	150611000	150611000
Trigger	6229.48	6229.48	6679390	6679390
$\geq 2$ loose $b$ -jets	503.552	467.146	2275760	2932620
$\geq 2$ light-jets	483.499	417.845	2189700	2671280
Tight $b$ -jet requirement	330.962	288.806	1490320	1640290
Forward jet requirement	51.843	40.8484	1186610	958414
$p_{Tbb} > 160\text{GeV}$	32.7426	26.7038	309454	259411

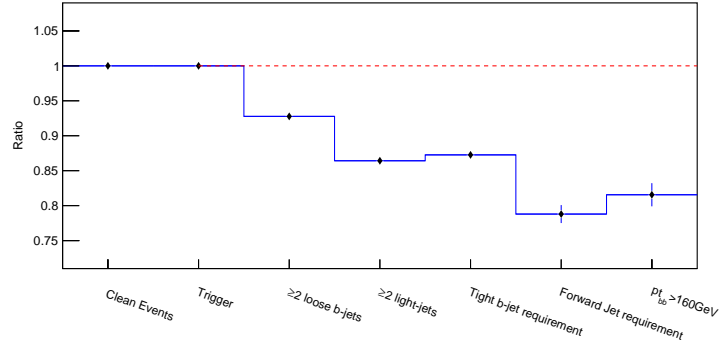


**Figure 6.1:** Ratio of the online event count over the offline event count for the Monte-Carlo simulations.

shown for the leading  $b$ -jet in Section 5.1, the offline jet is typically higher in  $p_T$  than the corresponding online jet. However the difference is small,  $\sim 2\%$ , so any effect on the cutflow should not be very pronounced.

The  $\sim 7\%$  drop on the light jet requirement is unexpected, as the requirement was solely for 2 non- $b$ -jets with  $p_T > 20$  GeV. Given the points above with respect to the  $p_T$  difference between online and offline, this drop should not be so severe. The fact the  $p_T$  cuts on the light jets were so low also suggests an anomalous result, as such a cut should not contribute a significant reduction in either online or offline events.

Following the drop for the light-jet cut, there is an unexpected increase in the online ratio following the tight  $b$ -tagging cut. As highlighted, the tagging efficiency was worse for online than offline, so any requirement for a tagged  $b$ -jet would be expected to produce a decrease in the online event count, relative to the offline count. Perhaps spuriously, the cutflow at this point corresponds to the 86% figure expected given the relative tagging efficiency for two  $b$ -jets.

The final drop occurs following the requirement for a high  $p_T$  forward jet. Figure 5.7 shows that for non- $b$ -jets in the forward region of the detector, the  $p_T$  of the offline jet is consistently higher than the online  $p_T$ . This difference would result in a drop in the online events, with fewer jets passing the threshold  $p_T$  cut compared to the offline events.

For the Monte-Carlo events, while the individual steps of the cutflow show some unusual results, the overall effect was an 18% reduction in the number of events that passed the VBF  $H \rightarrow b\bar{b}$  cuts.

### 6.1.2 Data

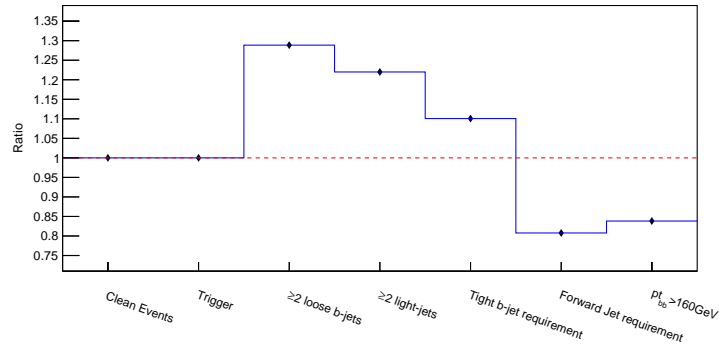


**Figure 6.2:** Ratio of the online event count over the offline event count for the data.

The cutflow performance in data shown in Figure 6.2 does not show the online event count being consistently lower than offline as demonstrated for the Monte-Carlo simulations in Figure 6.1. The overall effect of the cutflow for data described by Table 6.1 is a reduction in online events compared to offline events of  $\sim 84\%$ .

The first step shows a 25% increase in the number of events passing the loose  $b$ -jets cut online compared to offline. If the  $b$ -tagging is assumed to perform in the same way for data as for Monte-Carlo simulations, in that the differences between the MV2c10 and MV2c20 algorithms shown for the Monte-Carlo simulations (Figure 5.10) are consistent, a decrease would be expected after this cut, rather than an increase. However, the trigger applied to the data requires one tight  $b$ -jet, so simple extrapolations of efficiency differences between online and offline are not straightforward to understand. Additionally, the trigger required a  $b$ -jet with  $p_T > 80 \text{ GeV}$  and the loose selection required  $b$ -jets  $> 70 \text{ GeV}$ , meaning the offline results are skewed by trigger turn-on curves and different jet energy scale requirements.

Given the trigger selections (The  $b$ -jet identification and the  $p_T$  thresholds) are applied only in data, it is difficult to compare the relative normalisation of data and Monte-Carlo until the forward jet requirement is imposed (At which point all offline selections are in the plateau of the jet turn-on curve). After this requirement, both the data and Monte-Carlo show a ratio of  $\sim 0.8$ .

### 6.1.3 Summary of Cutflow Comparison for the VBF $H \rightarrow b\bar{b}$ events

The final reduction in online event count relative to the offline event count for the Monte-Carlo simulations was  $\sim 82\%$  of the offline event count, and  $\sim 84\%$  for the data. The results from individual steps in the cutflow are not supported by the results of Chapter 5, but these overall results, which are broadly consistent for both data and Monte-Carlo, are supported by the expected decrease in efficiency as a result of the different  $b$ -tagging algorithms. Looking only at the overall reduction at the final states suggests that future analyses may be able to apply TLA to the VBF  $H \rightarrow b\bar{b}$  channel to increase the final event yield.

With an average  $\sim 83\%$  reduction in event rate for the channel, usage of TLA at a rate of 2 kHz as described in Ref. [12] and Section 3.6, would result in an increase in output events of  $\sim 66\%$  compared to a standard offline analysis. This may not result in an increase in the signal from the analysis, but given the reduced bandwidth requirements of TLA, the trigger selections could be loosened to increase the signal efficiency. Analysis of this is beyond the scope of this dissertation.

This value is an estimate; there is additional computational cost involved with storing and computing the quantities required for TLA VBF  $H \rightarrow b\bar{b}$  analysis, such as the increased event size mentioned in Section 5.3.1 as a result of storing the  $b$ -tagging training quantities. Carrying out a rate analysis, to ensure the TLA can be applied in the VBF  $H \rightarrow b\bar{b}$  channel without decreasing the rate increase down to the point the final TLA event count is no longer an improvement, is a necessary step before approving TLA, but is beyond the scope of this dissertation.

## 6.2 Specific Jet Feature Distributions

While the previous chapter showed that the  $b$ -jets and non- $b$ -jets had slight differences that could be rectified for future analyses, the behaviour of those jets is sufficiently similar that plots of the kinematic quantities of the VBF  $H \rightarrow b\bar{b}$  jets can be made. The plots have been normalised to equal sums of weights to permit shape comparisons.

**Table 6.2:**  $m_{bb}$  bins defining an event as signal or background, along with the data source for the quantities.

Designation	$m_{bb}$ range / GeV	Sample
Background (Lower)	$m_{bb} < 100$	Data
Signal	$100 < m_{bb} < 140$	Monte-Carlo
Background (Upper)	$140 < m_{bb}$	Data

These plots are presented in signal and background regions, as defined by the  $m_{bb}$  value as shown in Table 6.2. The signal was plotted only using the Monte-Carlo simulation while the background regions were taken from data events. The kinematic quantities for leading  $b$ -jet and leading non- $b$ -jet of the VBF  $H \rightarrow b\bar{b}$  event are plotted for both the online and offline objects. The  $p_T$  distributions are shown in Figures 6.3 and 6.4 respectively, while the pseudorapidity plots are shown in Figure 6.5 and 6.6.

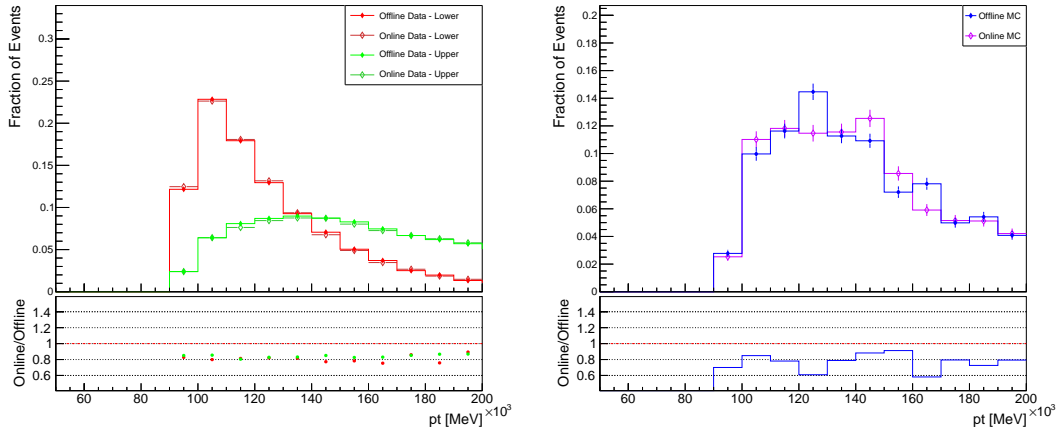


**Figure 6.3:**  $p_T$  distribution of the leading  $b$ -jet of the VBF  $H \rightarrow b\bar{b}$  event, plotted for both the background data regions in the left panel and Monte-Carlo signal events in the right panel.

The distribution of the  $p_T$  values for the leading  $b$ -jet shown in Figure 6.3 peaks at a higher value for the upper background region than the lower background region. This is a result of the  $m_{bb}$  sculpting the background distributions, as higher  $m_{bb}$  values will correlate

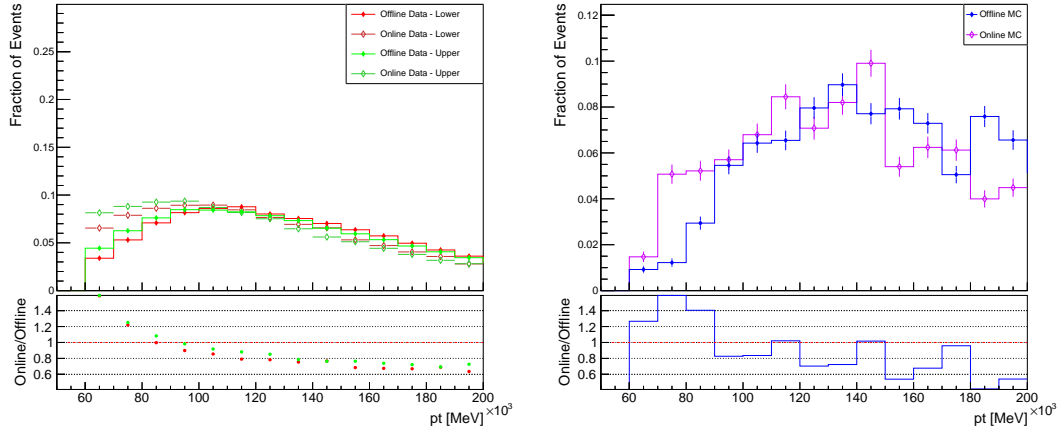


**Figure 6.4:**  $p_T$  distribution of the leading non- $b$ -jet of the VBF  $H \rightarrow b\bar{b}$  event, plotted for both the background data regions in the left panel and Monte-Carlo signal events in the right panel.

with higher  $b$ -jet  $p_T$  values. For the background  $p_T$  plot of the leading non- $b$ -jet, this sculpting is not seen as the  $p_T$  of the forward jet is not directly linked to the  $m_{bb}$  of the event. For both the leading  $b$ -jet and the leading non- $b$ -jet the online and offline distributions are similarly shaped for each of the defined  $m_{bb}$  regions.

For the leading  $b$ -jet, the ratio of the online to the offline events shown in Figure 6.3 is flat in both the upper and lower background regions, and has a value of  $\sim 0.8$ . This value is consistent with the expected decrease in the online event count shown in Figure 6.2. The Monte-Carlo signal plot shown in Figure 6.3, the line is insufficiently clear to make a firm statement but the ratio values are distributed around 0.8. For the leading non- $b$ -jet, the behaviour of the online/offline ratio is more complex, as shown by the distinct curve in the left panel of Figure 6.4. The online jets show a bias towards low  $p_T$  compared to the offline jets in both the upper and lower background regions, along with in the signal region. The relative ratio of the online and offline jets is affected by this, flattening out at a lower value of  $\sim 0.7$  than the expected 0.8 in both the background regions. This bias towards lower  $p_T$  events was seen in Figure 5.6 in the previous chapter showing the  $\frac{\Delta p_T}{p_T}$  distribution for the leading non- $b$ -jet. Figure 5.6 showed a large number of data jets with offline transverse momentum  $50 < p_T < 90$  GeV which had a  $\frac{\Delta p_T}{p_T}$  value between 0.1 and 0.2, indicating that for this region the offline  $p_T$  was significantly larger than the online. This observation is consistent with the left panel of Figure 6.4, as it suggests there will more online jets with  $50 < p_T < 80$  GeV than offline jets in the data, accounting for the shift in the distribution peaks. For the signal plot, Figure 5.6 did not show such a pronounced discrepancy for the

Monte-Carlo jets, only a slight increase of  $\frac{\Delta p_T}{p_T}$  values around 0.1 for this low  $p_T$  region, so such a shift is not absolutely expected for the signal region. In addition, as for the leading  $b$ -jet, a clear statement on the ratio of the Monte-Carlo events cannot be made, but the curve broadly follows the background ratios.

While there are differences between the signal and background regions and the small effects at low  $p_T$  in the leading non- $b$ -jets, for the complete  $p_T$  distributions of leading  $b$ -jet and most of the distribution for the leading non- $b$ -jet the offline jets performed the same as the online jets. This suggests that the online jet objects could be used in a TLA without any major effects on the outcome.

The plots for the same leading jet objects against  $\eta$  show the expected features for VBF  $H \rightarrow b\bar{b}$  jets. Figure 6.5 shows the pseudorapidity ranges for the  $b$ -jet confined to the central region of the detector where  $b$ -tagging is operational. The  $\eta$  plot for the leading non- $b$ -jet displays spikes of events with  $|\eta| \sim 3$ , which is expected given the requirements for a forward jet passing a  $p_T$  cut covered in Section 4.5. These features are present in both the signal and background regions.

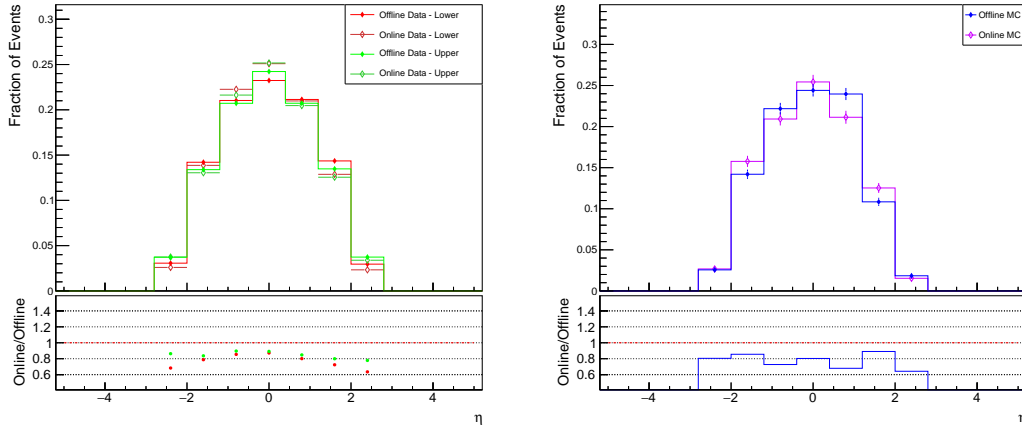


**Figure 6.5:**  $\eta$  distribution of the leading  $b$ -jet of the VBF  $H \rightarrow b\bar{b}$  event, plotted for both the background data regions in the left panel and Monte-Carlo signal events in the right panel.

The relative performance of online to offline shows some slight differences with respect to  $\eta$ . For the leading  $b$ -jet there is a noticeable peak in the ratio at  $\eta = 0$  for the lower signal region shown in Figure 6.5, however the upper signal region shows moderately consistent distribution around the expected 0.8 value. The signal  $\eta$  online/offline ratio has a larger degree of variation but is consistently around  $\sim 0.8$ . For the leading non- $b$ -jet shown in Figure 6.6 the ratio for the upper and lower background sectors is lower than expected in the



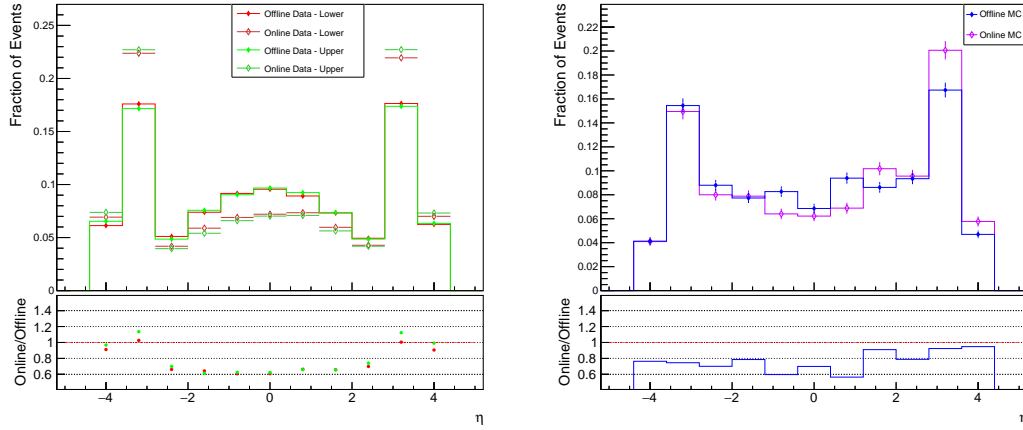


**Figure 6.6:**  $\eta$  distribution of the leading non- $b$ -jet of the VBF  $H \rightarrow b\bar{b}$  event, plotted for both the background data regions in the left panel and Monte-Carlo signal events in the right panel.

central region of the detector, but increases in the forward regions. For the signal sector, the distribution suggests a slight increase of the ratio at the outer  $\eta$  regions, but the difference is less pronounced than in the background regions.

Overall, the behaviour of the leading jets of the VBF  $H \rightarrow b\bar{b}$  event was fairly consistent for online and offline in most phase space regions. The plots showed the distribution features expected for the variables and the differences associated with the  $m_{bb}$  bins, along with showing agreement with the reduction in event number for online events. The discrepancy in online behaviour relative to the offline for the low  $p_T$  leading non- $b$ -jets can be explained by the observed differences in the non- $b$ -jet objects explored in the previous Chapter, however the cause of the improved relative performance of the online objects in the forward regions for the leading non- $b$ -jet are unknown. The upper background sector frequently had a higher ratio than the lower background sector, as shown across the entire  $p_T$  range in Figures 6.3 and 6.4. These observations suggest a TLA using these objects would show little change in the overall behaviour, and if the calibration steps suggested in Section 5.2.1 were applied, the differences in the online and offline behaviour may be removed.

### 6.3 Kinematic quantities of the VBF $H \rightarrow b\bar{b}$ event

Along with studying the kinematic quantities associated with single VBF  $H \rightarrow b\bar{b}$  jets, the kinematic properties of the jet pairs were compared for online and offline. For the non- $b$ -jet pair,  $p_{Tjj}$  and  $m_{jj}$  are plotted in Figures 6.7 and 6.8. Both of these variables are also training variables for the BDT used to refine the produced results (Appendix B). Figure 6.9 shows the  $p_{Tb\bar{b}}$  distribution and Figure 6.10 shows the  $m_{b\bar{b}}$  distribution.

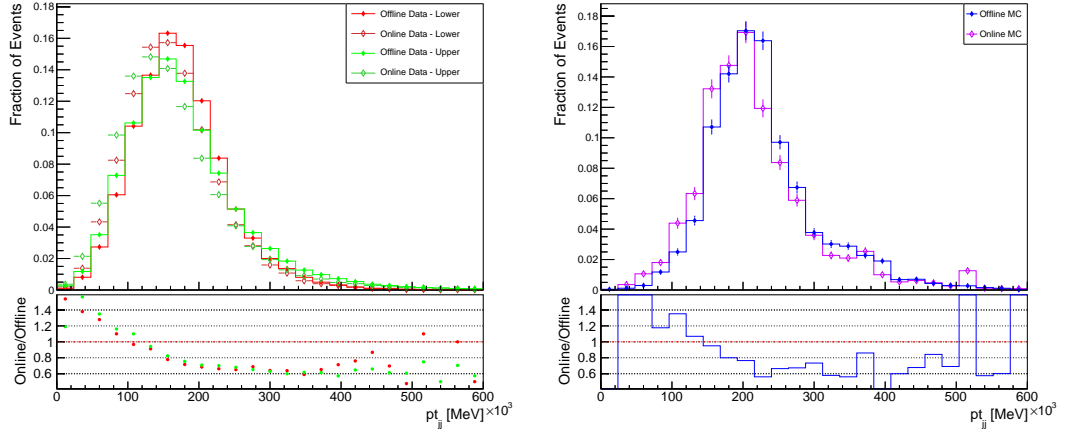


**Figure 6.7:**  $p_{Tjj}$  distribution for the online and offline VBF  $H \rightarrow b\bar{b}$  events, with background events from data shown in the left panel and Monte-Carlo signal events in the right.

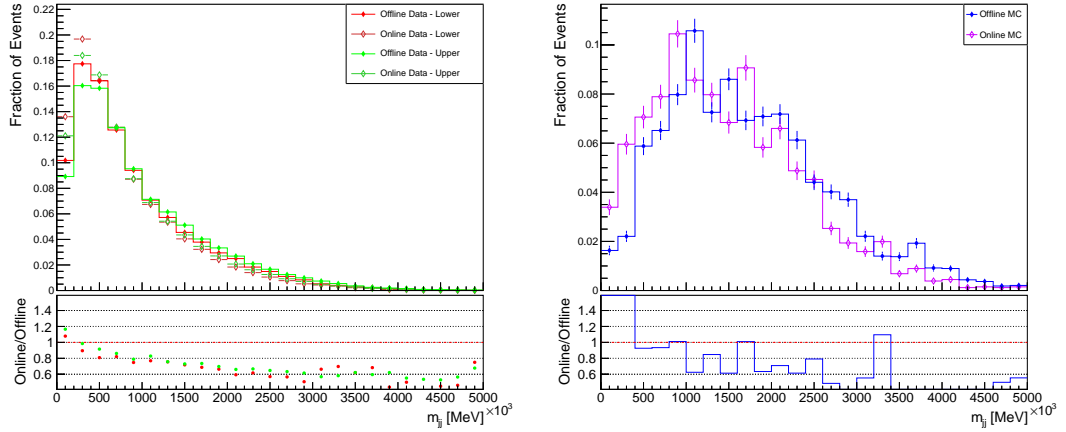


**Figure 6.8:**  $m_{jj}$  distribution for the online and offline VBF  $H \rightarrow b\bar{b}$  events, with background events from data shown in the left panel and Monte-Carlo signal events in the right.

The  $p_{Tjj}$  distributions shown in Figure 6.7 are similar to the plots of the leading non- $b$ -jet shown in Figure 6.4. The peak of the online distribution in the upper and lower background regions along with the signal region is shifted down in  $p_{Tjj}$  in relation to the offline region. The overall shape of the distribution is consistent between the Monte-Carlo simulations and the data background regions, and the ratio plot shows similar characteristics to that in Figure 6.4, flattening off at an online/offline ratio value of  $\sim 0.7$ . These features are replicated in the  $m_{jj}$  plot in Figure 6.8: similar distribution shapes for upper background, lower background and signal, increased numbers of online events compared to offline events at low  $m_{jj}$  (which corresponds to low non- $b$ -jet  $p_T$ ), the online/offline ratio flattening off to a value of  $\sim 0.7$ . These features, as described in Section 6.2, could be explained by the differences observed at low  $p_T$  regions for non- $b$ -jets in Section 5.2. Overall the performance of online is comparable to offline, so these variables may be used to train a BDT and perform any further analysis using TLA methodologies.

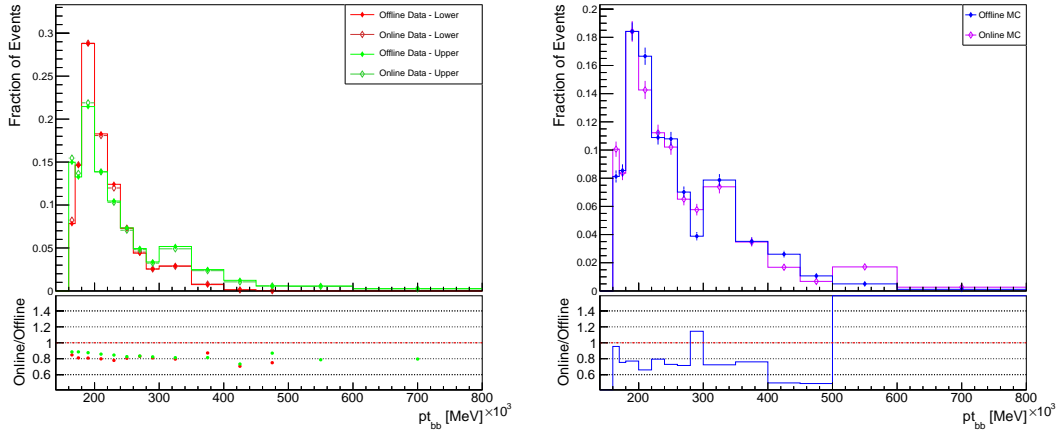


**Figure 6.9:**  $p_{Tbb}$  distribution for the online and offline VBF  $H \rightarrow b\bar{b}$  events, with background events from data shown in the left panel and Monte-Carlo signal events in the right.

The plots of  $p_{Tbb}$  in Figure 6.9 show excellent agreement between the online and offline objects. The ratio in the left panel of the Figure shows a flat line around  $\sim 0.8$ , in strong agreement with the reduction in event count shown in Figure 6.2. This agreement with the expected decrease is also shown in the signal events, which agree with Figure 6.1. For  $p_{Tbb}$ , the same behaviour is seen for online and offline jets, indicating there is no additional problems for applying a TLA beyond the rate reduction.

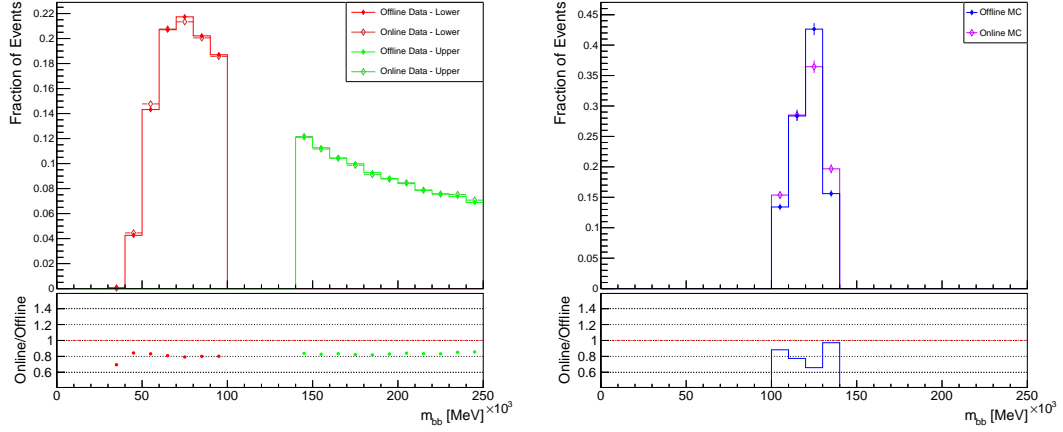


**Figure 6.10:**  $m_{bb}$  distribution for the online and offline VBF  $H \rightarrow b\bar{b}$  events, with background events from data shown in the left panel and Monte-Carlo signal events in the right.

The  $m_{bb}$  plot in Figure 6.10 for the background data events shows the online and offline analysis to be in good agreement. The online/offline ratio is a flat line at  $\sim 0.8$  as expected from the ratio plot in Figure 6.2. The behaviour of the upper and lower background region suggests a consistently decreasing function for  $m_{bb}$  beyond the peak at  $p_T \sim 80$  GeV, and look to link up across the signal region. The signal region is less clear than the background data, but suggests a ratio value of  $\sim 0.8$  and shows comparable behaviour for the online and offline jets. As for the other kinematic quantities in this section, the variables derived from the  $b\bar{b}$  pair look to behave consistently for online and offline and so could be used in a TLA.

## 6.4 BDT Input Variables

As discussed in Section 4.5, the full BDT analysis of the VBF  $H \rightarrow b\bar{b}$  search described in Appendix B was not performed for this dissertation. Given this is a critical component of the full Higgs search [11] in VBF  $H \rightarrow b\bar{b}$ , the performance of select BDT variables is explored for the signal and background regions described in Table 6.2. The variables  $m_{jj}$  and  $p_{Tjj}$  covered in the previous section are both BDT training variables.

This section covers  $\eta^*$ , given by

$$\eta^* = \frac{1}{2}(|\eta_{j1}| + |\eta_{j2}| - |\eta_{b1}| - |\eta_{b2}|), \quad (6.1)$$

which is plotted in Figure 6.11 for the online and offline events, and the  $p_{Tbalance}$ , given by

$$p_{Tbalance} = \frac{p_{Tj1} + p_{Tj2} + p_{Tb1} + p_{Tb2}}{p_{Tj1} + p_{Tj2} + p_{Tb1} + p_{Tb2}}, \quad (6.2)$$

which is shown in Figure 6.12.

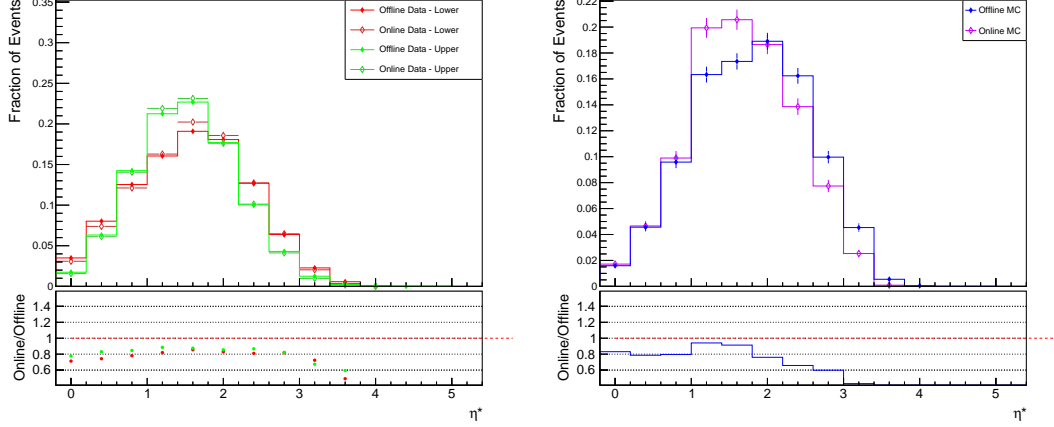


**Figure 6.11:**  $\eta^*$  distribution for the online and offline VBF  $H \rightarrow b\bar{b}$  events, with background events from data shown in the left panel and Monte-Carlo signal events in the right.

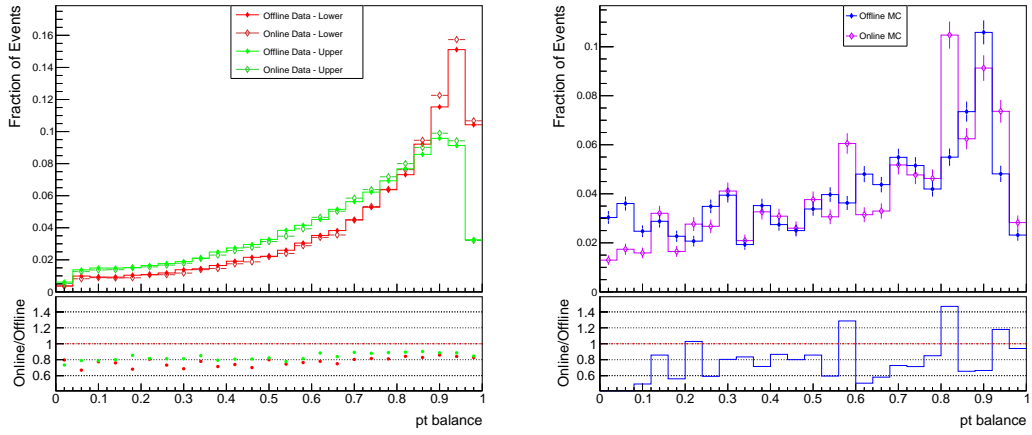


**Figure 6.12:**  $p_{Tbalance}$  distribution for the online and offline VBF  $H \rightarrow b\bar{b}$  events, with background events from data shown in the left panel and Monte-Carlo signal events in the right.

These variables behave in a consistent fashion as to the other VBF  $H \rightarrow b\bar{b}$  kinematic quantities covered in this section. For the lower background, upper background and signal sectors the shapes of the online and offline curves are comparable. The relative ratio of

the online to the offline events is  $\sim 0.8$ , as covered in Section 6.1 and shown clearly by the ratio plots in the left panels of Figures 6.11 and 6.12. The plots for the Monte-Carlo signal are less clear, but show a rough 20% decrease in online events compared to offline, and in general the upper background region performs better than the lower region.

Given the behaviour of the online and offline BDT quantities derived from the VBF  $H \rightarrow b\bar{b}$  event is similar, the trigger-level objects should perform comparably to the offline objects, and as such can be used in the training of a VBF  $H \rightarrow b\bar{b}$  BDT.

## 6.5 Summary

This chapter presents analysis and comparison of the VBF  $H \rightarrow b\bar{b}$  events obtained using trigger-level objects and offline reconstructions in data and Monte-Carlo simulation. The cutflows of the analysis for Monte-Carlo online, Monte-Carlo offline, data online and data offline were studied, and found to show online analysis produced  $\sim 82\%$  of the statistics of offline analysis for Monte-Carlo simulations, and  $\sim 84\%$  for data. These results are the overall decrease, the step by step changes of the cutflow were not predicted by the results from Chapter 5. Section 6.1 contains discussion of some possible causes, and they could also be the result of some coding bugs in the analysis.

With this reduction of event yield for a given analysis sample, the increased trigger rates permitted when applying TLA will result in an increased final event count. For current rate increases in TLA analyses [12], this would amount to an increase of  $\sim 66\%$  in the final number of events. This estimate of the possible increase does not consider any limitations on the rate that may result from increased computational demands on either processing or TLA object byte size.

To confirm that the TLA analysis would be possible with the trigger-level objects, the component jets, kinematic properties of the VBF  $H \rightarrow b\bar{b}$  event and select BDT training variables were investigated. These cases showed consistent behaviour between the online and offline objects in both background data and signal Monte-Carlo simulation, while showing the online rate decrease calculated from the cutflows.

These results suggest a full study of VBF  $H \rightarrow b\bar{b}$  analysis is a feasible proposal. Use of TLA could increase the output rate of the triggers to statistically significant levels and the objects produced will behave during analysis in a consistent fashion to the offline objects.

## CONCLUSIONS

This dissertation contains work done to test the feasibility of using Trigger-Object Level Analysis to improve the statistical significance of searches for the Higgs boson produced via Vector Boson Fusion and decaying to bottom quarks. This feasibility was tested by assessing the performance of trigger-level online analysis compared to the reconstructed offline analysis at two levels of abstraction for the VBF  $H \rightarrow b\bar{b}$  event, firstly at the resolution of comparing the performance for the individual jet objects that make up a VBF  $H \rightarrow b\bar{b}$  event separate from the VBF  $H \rightarrow b\bar{b}$  topology, and then by performing elements of the full VBF  $H \rightarrow b\bar{b}$  analysis with both online and offline objects to compare the performance.

The analysis was carried out using a vector boson fusion Monte-Carlo simulation sample and  $4.63 \text{ fb}^{-1}$  of data collected by the ATLAS detector during data-taking period D of the 2016  $\sqrt{s} = 13 \text{ TeV}$  Run.

The individual online and offline jet objects were shown to be comparable to each other, and could be improved to show a closer agreement in behaviour using standard ATLAS analysis tools. The positions of the  $b$ -jets and non- $b$ -jets that make up a VBF  $H \rightarrow b\bar{b}$  event were shown to agree within 1% of each other in  $(\eta, \phi)$  space. The  $p_T$  distributions of the online and offline jets demonstrated small differences, with offline  $p_T$  being  $\sim 5\%$  larger than online  $p_T$  for both the  $b$ -jets and the non- $b$ -jets. This  $p_T$  difference arises from a difference in the jet energy scale calibrations of the online and offline jet objects, and can be rectified in future analyses using standard jet calibration tools.

The  $b$ -tagging performance of the individual jet objects were compared, which showed differences in the  $b$ -tagging efficiency,  $c$ -jet rejection and light-jet rejection between the

online and offline jets. These differences in efficiency were consistent with the expected change in performance resulting from the different  $b$ -tagging algorithms applied to the online and offline jets. The 2016 MV2c10  $b$ -tagging algorithm to the offline reconstructed jets, while the  $b$ -tagging information for the online jets was calculated using the 2015 MV2c20 algorithm that was operational in the detector at that time. This suggests  $b$ -tagging performance of the online objects can be brought closer to agreement if the  $b$ -tagging training variables are preserved on the trigger-level objects, rather than being discarded and leaving only the  $b$ -tagging decision in the DxAOD. However, the performance of the algorithms underpinning the MV2 algorithms (Section 3.5.2) will also be improved over time, so the training variables will still differ from the offline reconstructions. In addition, the tracking will differ online to offline, so it is unlikely online performance could be brought to equivalence with offline performance.

Comparison of the online and offline performance in a VBF  $H \rightarrow b\bar{b}$  event phase space was then carried out. These cuts resulted in a final online event count that was reduced relative to the offline event count, with a final online event fraction of 82% for Monte-Carlo simulation and 84% for data. With the increased trigger rate permitted by using TLA, this would on average increase the final event number by 66% relative to a purely offline analysis.

Finally the VBF  $H \rightarrow b\bar{b}$  event specific objects, kinematic quantities and BDT training variables were compared for the online and offline events. For each separate variable, the performance of the online analysis was broadly consistent with respect to the offline analysis, taking into account the reduction in the number of online events highlighted during the cutflow analysis. These results suggest that TLA analysis in the VBF  $H \rightarrow b\bar{b}$  channel will provide increased statistical significance while providing comparable events to the full offline reconstructed analysis.

The work of this dissertation suggests certain additional studies outside the scope of this analysis should be carried out prior to approving TLA for the VBF  $H \rightarrow b\bar{b}$  channel. Primarily, the practicalities of applying TLA in the VBF  $H \rightarrow b\bar{b}$  channel require assessment. The solutions proposed in this dissertation to improve the agreement between the online and offline objects will increase the size of the trigger-objects output by the detector and may result in additional computational cost in the HLT. This may result in a smaller rate increase than assumed based on prior TLA studies and reduce or remove the improvement in rate suggested here. Another avenue for improving the agreement would be to run improved  $b$ -tagging, tracking and jet calibrations online to make it more comparable. Also, the increased trigger rate from a TLA may be sufficient even given the drop in efficiency with TLA.

In addition, the comparative behaviour of the online and offline objects could have further verification steps. This work did not implement trigger emulation in the Monte-Carlo



simulations, and this resulted in discrepancies between the Monte-Carlo and data results for the jet object performance. The full VBF  $H \rightarrow b\bar{b}$  analysis performed at  $\sqrt{s} = 8\text{TeV}$  carried out a BDT analysis after the cuts implemented in this dissertation to enhance the VBF  $H \rightarrow b\bar{b}$  phase space. Implementing or retraining a BDT was not possible within this dissertation, but would be an informative branch of further work to verify the feasibility. Finally, technical limitations prohibited making use of the full data set produced by the ATLAS detector, so analysis was carried out on a subset of the data. Greater statistical significance and a more certain statement of similarity could be made by performing the analysis for a larger dataset.

This study on the feasibility of performing TLA on the VBF  $H \rightarrow b\bar{b}$  channel search for the Higgs boson suggests that the trigger-level objects used for a VBF  $H \rightarrow b\bar{b}$  analysis are comparable to the offline objects, and that the similarity can be improved with some readily available calibrations and adjustments to the trigger-level objects. Also, the final VBF  $H \rightarrow b\bar{b}$  event produced using trigger-level objects will show a worse efficiency compared to offline reconstruction, but with the trigger rate increase afforded by TLA produce more events than an offline analysis. These additional events will be comparable in behaviour to the offline reconstruction. There are some additional sections of work relating to implementing and completely verifying the conclusions of this dissertation, but overall trigger-object level analysis is suggested as a feasible analysis strategy in the search for the Higgs boson via the VBF  $H \rightarrow b\bar{b}$  channel.

## CONFIGURATION

This appendix details the files and configuration settings used referenced throughout.

### A.1 Files

**Table A.1:** Full filenames of samples and other files used during the analysis

Title	Filename
2016 25ns Good Runs List	data16_13TeV.periodAllYear_DetStatus-v88-pro20-21_DQDefects00-02-04_PHYS_StandardGRL_All_Good_25ns.xml
2016 13TeV HIGG5D3 sample	data16_13TeV.{RUN_ID}.physics_Main.merge.DAOD_HIGG5D3.f715_m1620_p2689_tid{TID}
MC15C HIGG5D3 derivation Monte-Carlo sample	mc15_13TeV.341566.PowhegPythia8EvtGen_CT10_AZNLOCTEQ6L1_VBFH125_bb.merge.DAOD_HIGG5D3.e3988_s2726_r7772_r7676_p2719

## A.2 Configurations

**Table A.2:** Full names of configurations used during the analysis

Title	Name
Real Data 20.7 Jet Calibration Recommendations	JES_data2016_data2015_Recommendation_Dec2016.config
Monte-Carlo 20.7 Jet Calibration Recommendations	JES_MC15cRecommendation_May2016.config
January 2017 MV2c10 $b$ -tagging Recommendations	2016-20_7-13TeV-MC15-CDI-2017-01-31_v1.root
March 2016 MV2c20 $b$ -tagging Recommendations	2016-Winter-13TeV-MC15-CDI-March10_v1.root

## BOOSTED DECISION TREES

This appendix gives a brief description of the definition and use of Boosted Decision Trees (BDT), and provides specific details as to the training of a BDT for a VBF  $H \rightarrow b\bar{b}$  analysis.

### B.1 Machine Learning

A BDT is a machine learning technique that is applied in analyses to separate signal events from background events. The tree is trained on a particular training sample to build the decision logic and then applied to real data as required.

A decision tree as a structure operates by taking variables from the event and creating nodes with child nodes split on ranges of the variables. By assessing the relative signal/background proportions of the child nodes of this split node, the tree can create a split where one side is mostly signal and one mostly background. This process can be applied repeatedly to generate a multiple level tree of decision nodes, iteratively splitting sections of the event dataset. At a final terminating leaf node of the tree, the proportions of the signal and background events in the node will label it as a signal node or a background node.

This structure once trained, can be used to label a measured event by moving down the tree and evaluating each decision before a leaf node is reached in order to categorise the event. The boosting of a decision tree refers to the process of applying weights to the events. The tree will be iteratively produced, reweighting any misclassified events at each iterative stage to produce a more refined final tree [84]. Such structures are used throughout modern physics analyses at ATLAS [85].

## B.2 VBF $H \rightarrow b\bar{b}$ BDT Training

A detailed description of the BDT training that should be carried out for a VBF  $H \rightarrow b\bar{b}$  search is given in Ref. [11]. The event variables used for training the BDT on the VBF  $H \rightarrow b\bar{b}$  events are summarised here.

**Table B.1:** BDT Variables used in training for the VBF  $H \rightarrow b\bar{b}$  analysis.

Variable	Description
$M_{jj}$	Invariant mass of the VBF jet pair.
$p_{Tjj}$	Transverse momentum of the VBF jet pair
$\cos \theta$	Cosine of the polar angle of the cross product of the VBF jet momenta in the Higgs rest frame.
$Max(\eta)$	$max( \eta_{j1} ,  \eta_{j2} )$ Maximum of the two absolute pseudorapidity values for the VBF jets.
$\eta^*$	$\frac{1}{2}( \eta_{j1}  +  \eta_{j2}  -  \eta_{b1}  -  \eta_{b2} )$ Average pseudorapidity difference between the VBF and signal jets.
$min\Delta R_{j1}$	Minimum $(\eta, \phi)$ separation between the leading VBF jet and the closest other jet.
$min\Delta R_{j2}$	Minimum $(\eta, \phi)$ separation between the sub-leading VBF jet and the closest other jet.
QuarkGluonTagger( $j_1$ )	Number of tracks associated with the leading VBF jet [86].
QuarkGluonTagger( $j_2$ )	Number of tracks associated with the sub-leading VBF jet.
$p_T$ Balance	Ratio of vectorial and scalar sum of signal and VBF jets: $\frac{p_{Tj1} + p_{Tj2} + p_{Tb1} + p_{Tb2}}{p_{Tj1} + p_{Tj2} + p_{Tb1} + p_{Tb2}}$
$\Delta M_{jj}$	Difference in the largest invariant mass from all jet pairs and the invariant mass of the VBF jet pair

## BIBLIOGRAPHY

- [1] F. Englert and R. Brout, *Broken Symmetry and the Mass of Gauge Vector Mesons*, [Phys. Rev. Lett. \*\*13\*\* \(1964\) 321–323](#).
- [2] P. W. Higgs, *Broken Symmetries and the Masses of Gauge Bosons*, [Phys. Rev. Lett. \*\*13\*\* \(1964\) 508–509](#).
- [3] P. W. Higgs, *Broken symmetries, massless particles and gauge fields*, [Phys. Lett. \*\*12\*\* \(1964\) 132–133](#).
- [4] L. Evans and P. Bryant, *LHC Machine*, [JINST \*\*3\*\* \(2008\) S08001](#).
- [5] CMS Collaboration, S. Chatrchyan et al., *Observation of a new boson at a mass of 125 GeV with the CMS experiment at the LHC*, [Phys. Lett. \*\*B716\*\* \(2012\) 30–61](#), [arXiv:1207.7235 \[hep-ex\]](#).
- [6] ATLAS Collaboration, G. Aad et al., *Observation of a new particle in the search for the Standard Model Higgs boson with the ATLAS detector at the LHC*, [Phys. Lett. \*\*B716\*\* \(2012\) 1–29](#), [arXiv:1207.7214 \[hep-ex\]](#).
- [7] ATLAS, CMS Collaboration, G. Aad et al., *Combined Measurement of the Higgs Boson Mass in  $pp$  Collisions at  $\sqrt{s} = 7$  and 8 TeV with the ATLAS and CMS Experiments*, [Phys. Rev. Lett. \*\*114\*\* \(2015\) 191803](#), [arXiv:1503.07589 \[hep-ex\]](#).
- [8] LHC Higgs Cross Section Working Group Collaboration, S. Dittmaier et al., *Handbook of LHC Higgs Cross Sections: 1. Inclusive Observables*, [arXiv:1101.0593 \[hep-ph\]](#).
- [9] A. Djouadi, J. Kalinowski, and M. Spira, *HDECAY: A Program for Higgs boson decays in the standard model and its supersymmetric extension*, [Comput. Phys. Commun. \*\*108\*\* \(1998\) 56–74](#), [arXiv:hep-ph/9704448 \[hep-ph\]](#).
- [10] CMS Collaboration, V. Khachatryan et al., *Search for the standard model Higgs boson produced through vector boson fusion and decaying to  $b\bar{b}$* , [Phys. Rev. \*\*D92\*\* no. 3, \(2015\) 032008](#), [arXiv:1506.01010 \[hep-ex\]](#).

- [11] ATLAS Collaboration, M. Aaboud et al., *Search for the Standard Model Higgs boson produced by vector-boson fusion and decaying to bottom quarks in  $\sqrt{s} = 8$  TeV pp collisions with the ATLAS detector*, *JHEP* **11** (2016) 112, [arXiv:1606.02181 \[hep-ex\]](#).
- [12] ATLAS Collaboration Collaboration, *Search for light dijet resonances with the ATLAS detector using a Trigger-Level Analysis in LHC pp collisions at  $\sqrt{s} = 13$  TeV*, Tech. Rep. ATLAS-CONF-2016-030, CERN, Geneva, Jun, 2016.  
<https://cds.cern.ch/record/2161135>.
- [13] G. S. Brian R. Martin, *Particle Physics*. Wiley, Geneva, 2008.
- [14] Particle Data Group Collaboration, C. Patrignani et al., *Review of Particle Physics*, *Chin. Phys.* **C40** no. 10, (2016) 100001.
- [15] S. L. Glashow, *Partial Symmetries of Weak Interactions*, *Nucl. Phys.* **22** (1961) 579–588.
- [16] S. Weinberg, *A Model of Leptons*, *Phys. Rev. Lett.* **19** (1967) 1264–1266.
- [17] A. Salam, *Weak and Electromagnetic Interactions*, Conf. Proc. **C680519** (1968) 367–377.
- [18] T. D. Lee and C. N. Yang, *Question of Parity Conservation in Weak Interactions*, *Phys. Rev.* **104** (1956) 254–258.  
<https://link.aps.org/doi/10.1103/PhysRev.104.254>.
- [19] N. Cabibbo, *Unitary Symmetry and Leptonic Decays*, *Phys. Rev. Lett.* **10** (1963) 531–533. [,648(1963)].
- [20] M. Kobayashi and T. Maskawa, *CP Violation in the Renormalizable Theory of Weak Interaction*, *Prog. Theor. Phys.* **49** (1973) 652–657.
- [21] L.-L. Chau and W.-Y. Keung, *Comments on the Parametrization of the Kobayashi-Maskawa Matrix*, *Phys. Rev. Lett.* **53** (1984) 1802.
- [22] ATLAS Collaboration, G. Aad et al., *Observation of a new particle in the search for the Standard Model Higgs boson with the ATLAS detector at the LHC*, *Phys. Lett.* **B716** (2012) 1–29, [arXiv:1207.7214 \[hep-ex\]](#).
- [23] CMS Collaboration, S. Chatrchyan et al., *Observation of a new boson at a mass of 125 GeV with the CMS experiment at the LHC*, *Phys. Lett.* **B716** (2012) 30–61, [arXiv:1207.7235 \[hep-ex\]](#).
- [24] J. M. Campbell, J. W. Huston, and W. J. Stirling, *Hard Interactions of Quarks and Gluons: A Primer for LHC Physics*, *Rept. Prog. Phys.* **70** (2007) 89, [arXiv:hep-ph/0611148 \[hep-ph\]](#).

- [25] NNPDF Collaboration, R. D. Ball et al., *Parton distributions for the LHC Run II*, **JHEP** **04** (2015) 040, [arXiv:1410.8849 \[hep-ph\]](#).
- [26] J. C. Collins, *Light cone variables, rapidity and all that*, [arXiv:hep-ph/9705393 \[hep-ph\]](#).
- [27] M. H. Seymour and M. Marx, *Monte Carlo Event Generators*, pp. , 287–319. 2013. [arXiv:1304.6677 \[hep-ph\]](#).  
<https://inspirehep.net/record/1229804/files/arXiv:1304.6677.pdf>.
- [28] T. Sjostrand et al., *An Introduction to PYTHIA 8.2*, **Comput. Phys. Commun.** **191** (2015) 159–177, [arXiv:1410.3012 \[hep-ph\]](#).
- [29] T. Gleisberg et al., *Event generation with SHERPA 1.1*, **JHEP** **02** (2009) 007, [arXiv:0811.4622 \[hep-ph\]](#).
- [30] C. Oleari, *The POWHEG-BOX*, **Nucl. Phys. Proc. Suppl.** **205-206** (2010) 36–41, [arXiv:1007.3893 \[hep-ph\]](#).
- [31] B. Andersson, G. Gustafson, G. Ingelman, and T. Sjostrand, *Parton fragmentation and string dynamics*, **Physics Reports** **97** no. 2, (1983) 31 – 145.  
<http://www.sciencedirect.com/science/article/pii/0370157383900807>.
- [32] B. R. Webber, *A QCD Model for Jet Fragmentation Including Soft Gluon Interference*, **Nucl. Phys.** **B238** (1984) 492–528.
- [33] P. Z. Skands, *Tuning Monte Carlo Generators: The Perugia Tunes*, **Phys. Rev.** **D82** (2010) 074018, [arXiv:1005.3457 \[hep-ph\]](#).
- [34] P. Skands, S. Carrazza, and J. Rojo, *Tuning PYTHIA 8.1: the Monash 2013 Tune*, **Eur. Phys. J.** **C74** no. 8, (2014) 3024, [arXiv:1404.5630 \[hep-ph\]](#).
- [35] M. Y. Hussein, *Higgs Boson Production at the LHC*, [arXiv:1703.03952 \[hep-ph\]](#).
- [36] ATLAS, CMS Collaboration, G. Mila, *Higgs searches at LHC*, eConf **C080625** (2008) 0031.
- [37] ATLAS Collaboration, G. Aad et al., *Search for the Standard Model Higgs boson produced in association with a vector boson and decaying to a b-quark pair with the ATLAS detector*, **Phys. Lett.** **B718** (2012) 369–390, [arXiv:1207.0210 \[hep-ex\]](#).
- [38] ATLAS Collaboration, M. Aaboud et al., *Evidence for the associated production of the Higgs boson and a top quark pair with the ATLAS detector*, **Phys. Rev.** **D97** no. 7, (2018) 072003, [arXiv:1712.08891 \[hep-ex\]](#).
- [39] Particle Data Group Collaboration, C. Patrignani et al., *Review of Particle Physics - Status of the Higgs Boson*, **Chin. Phys.** **C40** no. 10, (2016) 100001.



- [40] ATLAS Collaboration, G. Aad et al., *Measurement of the Higgs boson mass from the  $H \rightarrow \gamma\gamma$  and  $H \rightarrow ZZ^* \rightarrow 4\ell$  channels with the ATLAS detector using  $25 \text{ fb}^{-1}$  of  $pp$  collision data*, *Phys. Rev. D* **90** no. 5, (2014) 052004, [arXiv:1406.3827 \[hep-ex\]](#).
- [41] ATLAS Collaboration, G. Aad et al., *Search for the Higgs boson in the  $H \rightarrow WW(*) \rightarrow \ell_\nu \ell_\nu$  decay channel in  $pp$  collisions at  $\sqrt{s} = 7 \text{ TeV}$  with the ATLAS detector*, *Phys. Rev. Lett.* **108** (2012) 111802, [arXiv:1112.2577 \[hep-ex\]](#).
- [42] ATLAS Collaboration, *Measurements of the properties of the Higgs-like boson in the two photon decay channel with the ATLAS detector using  $25 \text{ fb}^{-1}$  of proton-proton collision data*,.
- [43] ATLAS Collaboration, M. Aaboud et al., *Search for the Standard Model Higgs boson produced in association with top quarks and decaying into a  $b\bar{b}$  pair in  $pp$  collisions at  $\sqrt{s} = 13 \text{ TeV}$  with the ATLAS detector*, [arXiv:1712.08895 \[hep-ex\]](#).
- [44] S. L. Glashow, D. V. Nanopoulos, and A. Yildiz, *Associated Production of Higgs Bosons and Z Particles*, *Phys. Rev. D* **18** (1978) 1724–1727.
- [45] S. Asai et al., *Prospects for the search for a standard model Higgs boson in ATLAS using vector boson fusion*, *Eur. Phys. J. C* **32S2** (2004) 19–54, [arXiv:hep-ph/0402254 \[hep-ph\]](#).
- [46] *LEP design report*. CERN, Geneva, 1983. <https://cds.cern.ch/record/98881>. By the LEP Injector Study Group.
- [47] *LEP design report*. CERN, Geneva, 1984. <https://cds.cern.ch/record/102083>. Copies shelved as reports in LEP, PS and SPS libraries.
- [48] ATLAS Collaboration, G. Aad et al., *The ATLAS Experiment at the CERN Large Hadron Collider*, *JINST* **3** (2008) S08003.
- [49] CMS Collaboration, S. Chatrchyan et al., *The CMS Experiment at the CERN LHC*, *JINST* **3** (2008) S08004.
- [50] LHCb Collaboration, A. A. Alves, Jr. et al., *The LHCb Detector at the LHC*, *JINST* **3** (2008) S08005.
- [51] ALICE Collaboration, K. Aamodt et al., *The ALICE experiment at the CERN LHC*, *JINST* **3** (2008) S08002.
- [52] Y. Koshiha et al., *Luminosity Increase in Laser-Compton Scattering by Crab Crossing Method*, in *Proc. of International Particle Accelerator Conference (IPAC'17), Copenhagen, Denmark, 14-19 May, 2017*, pp. , 902–904. JACoW, Geneva, Switzerland, May, 2017. <http://jacow.org/ipac2017/papers/mopva023.pdf>. <https://doi.org/10.18429/JACoW-IPAC2017-MOPVA023>.

- [53] J. Pequeno, “Computer generated image of the whole ATLAS detector.”  
<https://cds.cern.ch/record/1095924>. Accessed 03/09/2017.
- [54] ATLAS Collaboration Collaboration, *ATLAS inner detector: Technical Design Report, 1*. Technical Design Report ATLAS. CERN, Geneva, 1997.  
<https://cds.cern.ch/record/331063>.
- [55] H. Wilkens and the ATLAS LArg Collaboration, *The ATLAS Liquid Argon calorimeter: An overview*, Journal of Physics: Conference Series **160** no. 1, (2009) 012043. <http://stacks.iop.org/1742-6596/160/i=1/a=012043>.
- [56] ATLAS Collaboration, A. M. Henriques Correia, *The ATLAS Tile Calorimeter*, Tech. Rep. ATL-TILECAL-PROC-2015-002, CERN, Geneva, Mar, 2015.  
<https://cds.cern.ch/record/2004868>.
- [57] A. Artamonov et al., *The ATLAS Forward Calorimeter*, Journal of Instrumentation **3** no. 02, (2008) P02010. <http://stacks.iop.org/1748-0221/3/i=02/a=P02010>.
- [58] ATLAS Collaboration, M. zur Nedden, *The Run-2 ATLAS Trigger System: Design, Performance and Plan*, Tech. Rep. ATL-DAQ-PROC-2016-039, CERN, Geneva, Dec, 2016. <https://cds.cern.ch/record/2238679>.
- [59] ATLAS Collaboration, M. Aaboud et al., *Performance of the ATLAS Trigger System in 2015*, *Eur. Phys. J. C* **77** no. 5, (2017) 317, [arXiv:1611.09661](https://arxiv.org/abs/1611.09661) [hep-ex].
- [60] R. Achenbach et al., *The ATLAS level-1 calorimeter trigger*, *JINST* **3** (2008) P03001.
- [61] ATLAS Collaboration, *Trigger Menu in 2016*, Tech. Rep. ATL-DAQ-PUB-2017-001, CERN, Geneva, Jan, 2017. <https://cds.cern.ch/record/2242069>.
- [62] G. P. Salam, *Towards Jetography*, *Eur. Phys. J. C* **67** (2010) 637–686,  
[arXiv:0906.1833](https://arxiv.org/abs/0906.1833) [hep-ph].
- [63] R. Atkin, *Review of jet reconstruction algorithms*, *J. Phys. Conf. Ser.* **645** no. 1, (2015) 012008.
- [64] M. Cacciari, G. P. Salam, and G. Soyez, *The Anti-k(t) jet clustering algorithm*, *JHEP* **04** (2008) 063, [arXiv:0802.1189](https://arxiv.org/abs/0802.1189) [hep-ph].
- [65] O. Lundberg, *Calibration Systems of the ATLAS Tile Calorimeter*, pp. , 399–402. 2012. [arXiv:1212.3676](https://arxiv.org/abs/1212.3676) [physics.ins-det].  
<https://inspirehep.net/record/1207575/files/arXiv:1212.3676.pdf>.
- [66] G. Pospelov and the Atlas Hadronic Calibration Group, *The overview of the ATLAS local hadronic calibration*, Journal of Physics: Conference Series **160** no. 1, (2009) 012079. <http://stacks.iop.org/1742-6596/160/i=1/a=012079>.

- [67] Z. Marshall and the ATLAS Collaboration, *Simulation of Pile-up in the ATLAS Experiment*, Journal of Physics: Conference Series **513** no. 2, (2014) 022024.  
<http://stacks.iop.org/1742-6596/513/i=2/a=022024>.
- [68] *Tagging and suppression of pileup jets with the ATLAS detector*, Tech. Rep. ATLAS-CONF-2014-018, CERN, Geneva, May, 2014.  
<https://cds.cern.ch/record/1700870>.
- [69] ATLAS Collaboration, *Performance of b-Jet Identification in the ATLAS Experiment*, JINST **11** no. 04, (2016) P04008, [arXiv:1512.01094](https://arxiv.org/abs/1512.01094) [hep-ex].
- [70] *Expected performance of the ATLAS b-tagging algorithms in Run-2*, Tech. Rep. ATL-PHYS-PUB-2015-022, CERN, Geneva, Jul, 2015.  
<https://cds.cern.ch/record/2037697>.
- [71] ATLAS Collaboration, *Optimisation of the ATLAS b-tagging performance for the 2016 LHC Run*, ATL-PHYS-PUB-2016-012 (2016).  
<https://cds.cern.ch/record/2160731>.
- [72] ATLAS Collaboration, *Commissioning of the ATLAS high-performance b-tagging algorithms in the 7 TeV collision data*, Tech. Rep. ATLAS-CONF-2011-102, CERN, Geneva, Jul, 2011. <http://cds.cern.ch/record/1369219>.
- [73] R. Fruhwirth, *Application of Kalman filtering to track and vertex fitting*, Nucl. Instrum. Meth. **A262** (1987) 444–450.
- [74] I. Antcheva et al., *ROOT A C++ framework for petabyte data storage, statistical analysis and visualization*, Computer Physics Communications **180** no. 12, (2009) 2499 – 2512.  
<http://www.sciencedirect.com/science/article/pii/S0010465509002550>.
- [75] J. Catmore et al., *A new petabyte-scale data derivation framework for ATLAS*, Journal of Physics: Conference Series **664** no. 7, (2015) 072007.  
<http://stacks.iop.org/1742-6596/664/i=7/a=072007>.
- [76] R. Seuster, M. Elsing, G. A. Stewart, and V. Tsulaia, *Status and Future Evolution of the ATLAS Offline Software*, Journal of Physics: Conference Series **664** no. 7, (2015) 072044. <http://stacks.iop.org/1742-6596/664/i=7/a=072044>.
- [77] C. Eck et al., *LHC computing Grid: Technical Design Report. Version 1.06* (20 Jun 2005). Technical Design Report LCG. CERN, Geneva, 2005.  
<https://cds.cern.ch/record/840543>.
- [78] J. Pumplin et al., *New generation of parton distributions with uncertainties from global QCD analysis*, JHEP **07** (2002) 012, [arXiv:hep-ph/0201195](https://arxiv.org/abs/hep-ph/0201195) [hep-ph].

- [79] ATLAS Collaboration, G. Aad et al., *Measurement of the  $Z/\gamma^*$  boson transverse momentum distribution in  $pp$  collisions at  $\sqrt{s} = 7$  TeV with the ATLAS detector*, [JHEP \*\*09\*\* \(2014\) 145](#), [arXiv:1406.3660 \[hep-ex\]](#).
- [80] S. Agostinelli et al., *Geant4a simulation toolkit*, [Nuclear Instruments and Methods in Physics Research Section A: Accelerators, Spectrometers, Detectors and Associated Equipment \*\*506\*\* no. 3, \(2003\) 250 – 303](#).  
<http://www.sciencedirect.com/science/article/pii/S0168900203013688>.
- [81] ATLAS Collaboration, G. Aad et al., *The ATLAS Simulation Infrastructure*, [Eur. Phys. J. \*\*C70\*\* \(2010\) 823–874](#), [arXiv:1005.4568 \[physics.ins-det\]](#).
- [82] ATLAS Collaboration, M. Aaboud et al., *Jet energy scale measurements and their systematic uncertainties in proton-proton collisions at  $\sqrt{s} = 13$  TeV with the ATLAS detector*, [Phys. Rev. \*\*D96\*\* no. 7, \(2017\) 072002](#), [arXiv:1703.09665 \[hep-ex\]](#).
- [83] A. Schwartzman, *Jet energy calibration at the LHC*, [Int. J. Mod. Phys. \*\*A30\*\* no. 31, \(2015\) 1546002](#), [arXiv:1509.05459 \[hep-ex\]](#).
- [84] B. P. Roe, H.-J. Yang, J. Zhu, Y. Liu, I. Stancu, and G. McGregor, *Boosted decision trees, an alternative to artificial neural networks*, [Nucl. Instrum. Meth. \*\*A543\*\* no. 2-3, \(2005\) 577–584](#), [arXiv:physics/0408124 \[physics\]](#).
- [85] M. Paganini, *Machine Learning Algorithms for  $b$ -Jet Tagging at the ATLAS Experiment*, in *18th International Workshop on Advanced Computing and Analysis Techniques in Physics Research (ACAT 2017) Seattle, WA, USA, August 21-25, 2017*. 2017. [arXiv:1711.08811 \[hep-ex\]](#).  
<https://inspirehep.net/record/1638366/files/arXiv:1711.08811.pdf>.
- [86] J. Gallicchio and M. D. Schwartz, *Quark and Gluon Tagging at the LHC*, [Phys. Rev. Lett. \*\*107\*\* \(2011\) 172001](#), [arXiv:1106.3076 \[hep-ph\]](#).